

MOSES: MHT Optical Star and Exoplanet Survey

Amar Singh Rambukwella-Gill

A THESIS SUBMITTED IN PARTIAL FULFILMENT
OF THE REQUIREMENTS FOR THE DEGREE OF
MASTER OF SCIENCE

Jeremiah Horrocks Institute for Mathematics, Physics and Astronomy
University of Central Lancashire

January 2020

Declaration

Type of Award: Master of Science

School: Physical Sciences and Computing

I declare that while registered as a candidate for the research degree, I have not been a registered candidate or enrolled student for another award of the University or other academic or professional institution.

I declare that no material contained in the thesis has been used in any other submission for an academic award and is solely my own work.

No proof-reading service was used in the compilation of this thesis.

Amar Singh Rambukwella-Gill

January 2020

Abstract

This thesis presents the design and instigation of a new optical imaging survey to search for stellar variability, exoplanets and solar system bodies. The data collection was carried out using the Moses Holden Telescope based at Alston Observatory, Preston UK. Over the course of 183 nights from our first observing season and 3 nights from our second season (with actual observing achieved on 25 nights from season 1) the survey obtained 3728 images, and obtained at least 200 repeat observations for 29,399 objects. Preliminary analysis indicates a total of 430 stars display variability above 3σ , thereby increasing the number of known variables in the survey region by a factor of at least 200. Ongoing observations and analysis will classify the various forms of variability, and further push down the thresholds for detection of variability to allow the detection of transiting exoplanets.

Contents

Declaration	ii
Abstract	iii
Acknowledgements	vii
1 Introduction/Variable Objects	1
1.1 Transiting Objects	1
1.1.1 Transit Photometry	2
1.2 Variable Objects	4
1.2.1 Intrinsically Variable Stars	7
1.2.2 Extrinsically Variable Stars	13
1.3 Moving Objects	14
2 Existing/Previous Exoplanet Surveys	15
2.1 The Kepler Mission	15
2.1.1 K2 Mission	16
2.2 The WASP Project	16
2.3 Evryscope	17
2.4 TESS	18
3 MOSES Project Hardware	19

3.1	The Moses Holden Telescope	19
3.2	The CCD & Filter Set	20
3.3	Software	21
4	Observations	23
4.1	Analysis of Exoplanet Archive Data	23
4.2	Survey Field Selection	24
4.3	Observing Strategy	26
4.4	The Reduction Pipeline	30
4.4.1	Calibration Frames	31
4.4.2	Astrometry	31
4.5	Post-reduction Calibration	32
4.5.1	Border Pixel Removal	32
4.5.2	Vingette Correction	34
4.5.3	Differential Photometry	35
5	The Catalogue	38
5.1	Aperture Photometry	38
5.2	Previously Detected Variables	39
5.3	Data Cut	40
5.4	Finding Variability	41
6	Discussion	43
6.1	Suggested Improvements to Survey Strategy	44
6.2	MOSES Season 1	46
6.3	Eclipsing Binary	47
6.4	Cepheid	48
6.5	Mira	48
6.6	Eclipsing Contact Binary	49

6.7	Unknown Variability	50
7	Conclusion	52
7.1	Future Work	52
A	Appendix	57
B	Variable Light Curves	62

Acknowledgements

I would like to firstly thank my supervisor Dr Mark Norris for his invaluable advice and guidance throughout this project. He has made me develop my own skills and abilities even when I did not think it was possible. I would like to thanks the University of Central Lancashire for allowing myself use the Moses Holden Telescope for my research. I would also like to thank the staff within the JHI for their help through this project.

I would also like to thanks my Mum, Kris Rambukwella-Gill, my Dad, Deleep Gill and my Sister, Nisha Rambukwella-Gill for their support they have given me throughout my entire time at university, allowing me continue my education into the field of Astrophysics.

Chapter 1

Introduction/Variable Objects

Chapter 1 presents an introduction into the different types of variability that have been or may be encountered during the ongoing MOSES project. Variable objects are a fascinating and crucial part of astrophysics, providing key insights into the inner workings of stars, as well as providing more practical information such as methods to estimate distances to stars and galaxies.

1.1 Transiting Objects

The MOSES project is designed to find variable astronomical objects including new exoplanets using the transit method. However, in order to securely claim detection of an exoplanet we must also rule out alternative phenomena which result in variability such as eclipsing binaries and starspots. Starspots can be distinguished with follow-up observations (observing multiple transits) as they are not constant and over time individual starspots will fade. With binary systems, analysing the light curve should reveal a distinct second dip (caused by the eclipse of the fainter star) that would not otherwise be seen with most planet transits, the magnitude and duration would also be distinctly different to that of a planet. The decrease in luminosity during a binary transit is also much larger than that of a planet, due to the fact that the occulting

CHAPTER 1

star in an eclipsing binary would be much larger than any planet. Using the Kepler space telescope the first Kepler mission looked at $\sim 100,000$ stars (Borucki et al., 2003). Within this sample 1052 had an exoplanet with a period ≤ 10 days, similar to the periods expected to be detected by our survey given its duration and cadence. We would expect a similar distribution of periods for the exoplanets within our field. The host stars of the 1052 Kepler exoplanets have a magnitude range of $8.5 \leq V \leq 17.5$ mag. During the survey, it will not be possible to survey continuously every night. In order to classify a variable with a sparse light curve a form of analysis will have to be performed to help classify the variability seen.

1.1.1 Transit Photometry

Transit photometry is the method of observing the minute dip (typically $< 1\%$) in the observed output of light from a star as an orbiting planet passes across the face of the star relative to the observer. If the dimming is found to be of the same depth each event and the depth indicates a planet sized object is occulting the star and periodic, then it is highly likely that there is an orbiting planet around the star. The amount the light fractionally dips during a transit. This fraction is indicative of the size ratio between the planet and star. To increase the chance of finding a transiting planet, surveys must image as often as possible over long periods of time over as large an area of the sky as possible. This strongly influenced the survey design of this survey as we discuss in detail in Section 4.3.

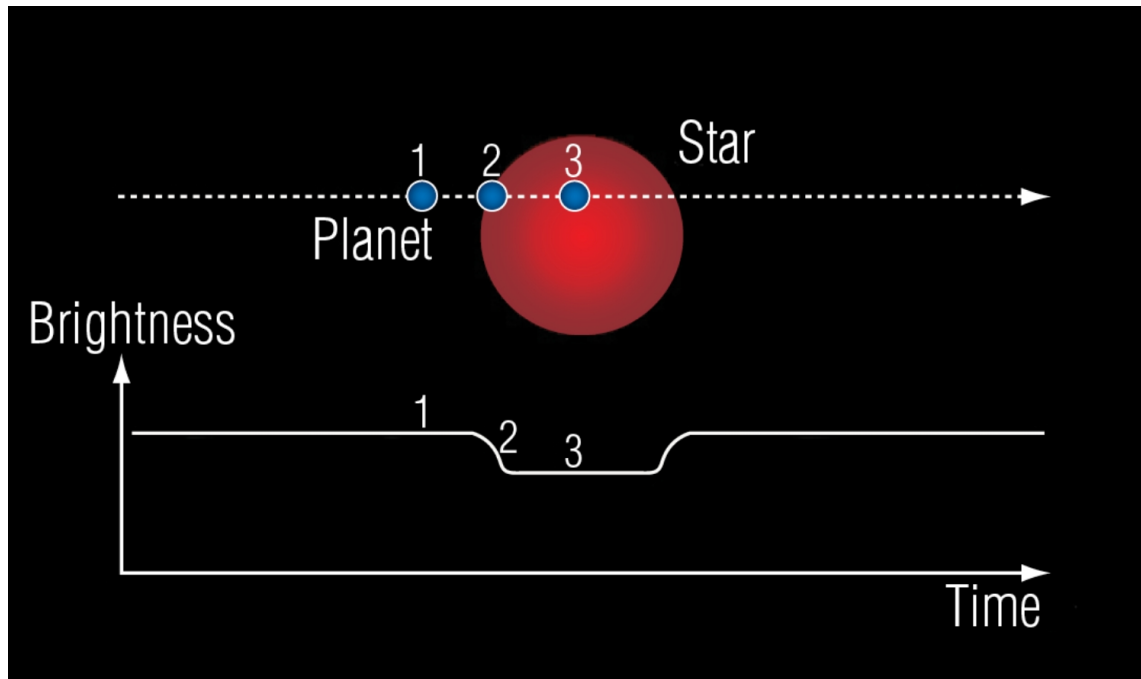


Figure 1.1: A graphic representation of a light curve as planet transits across the host star. (NASA, ESA, G. Bacon (STSci)).

From Figure 1.1, we can see that there are three stages to a transit. The first stage is where the planet does not block any of the star's light. The second stage is where the planet begins to transit across the star and a dip in the light from the star begins. By stage three the planet is completely in front of the star and is blocking the maximum amount of light. The first two stages then repeat in reverse as the planet ends its transit across the star.

Advantages

Transit photometry is the most efficient method of exoplanet detection. It also provides physical information about the planet, as the size of the host star can be estimated (based on its observed stellar type), the size of the exoplanet can be determined by the amount of light that is blocked during a transit as the decrease in the star's luminosity is proportional to exoplanet size. When a planet's photometry and

CHAPTER 1

radial velocity data (obtained separately) is combined an estimate for the mass and density of the planet can be obtained. A planet's transit can also provide information about atmospheric conditions of the planet, through spectroscopic observations. By subtracting the star's spectrum from the total system the transmission spectrum of the planet's atmosphere can be determined. Photometry can be taken from both ground and space based survey missions such as WASP or Kepler (Pollacco et al., 2006) (Borucki et al., 2003).

Disadvantages

For this method to be effective a transit must occur, so the planet, star and observer must all align. Only $\sim 10\%$ of planets with short orbital periods experience such an alignment, and this decreases further for planets with longer orbital periods and hence larger radii orbits (Williams, 2017). Another issue is that a planet's transit duration can be very short compared to its orbital period. A transit may only last a few hours, yet the orbit of the planet may take months to years. To confirm that there is an exoplanet more than one transit must be observed, ideally more than three. Mis-identification is also an issue as non-planetary bodies in orbit, such as Brown Dwarfs (BDs) or cometary dust, could be falsely classified as exoplanet systems.

1.2 Variable Objects

Alongside searching for exoplanets we have also detected and attempted to classify various forms of stellar variability. A description of the different types of stellar variability is given in this section as it is crucial to understand the types of variability we have encountered and will encounter as the survey continues. There are two main classification of variable stars; Intrinsically variable stars (IVS) and Extrinsically variable stars (EVS).

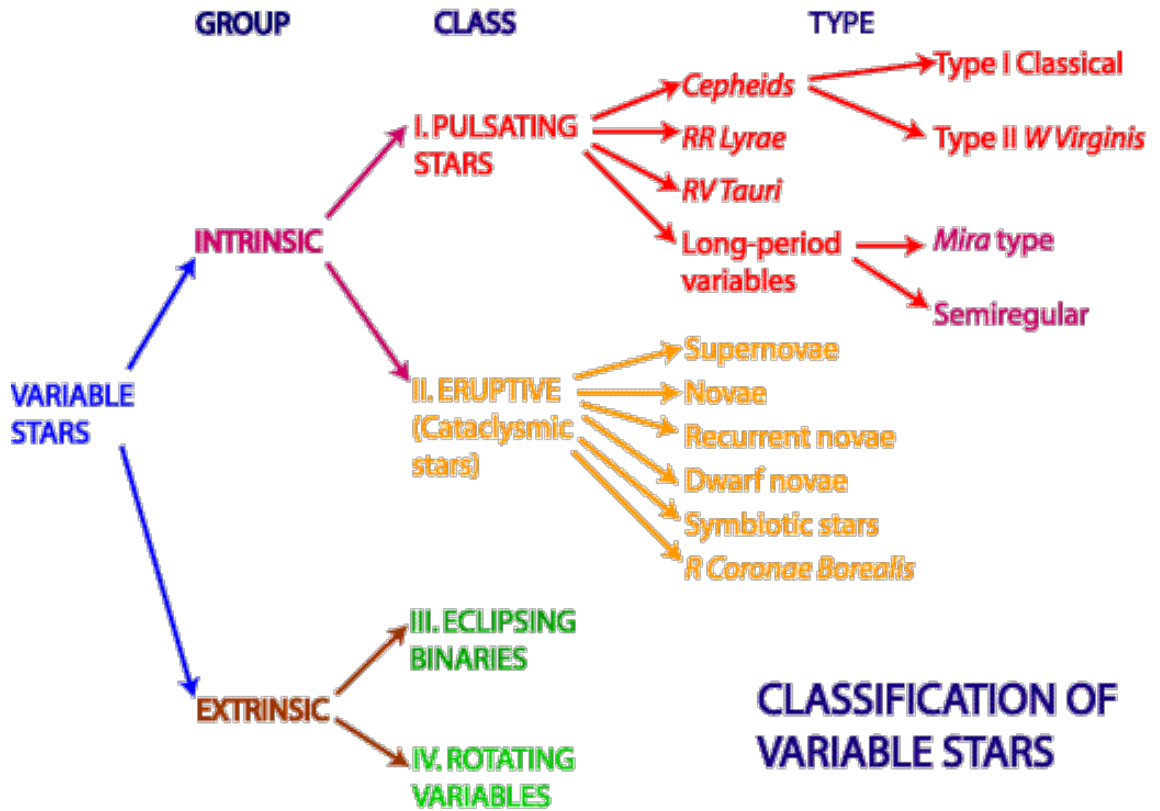


Figure 1.2: Classification of Variable Stars (ANTF, 2018)

From Figure 1.2 we see that within the two main groups of variable stars there are different types and classes of variable, these all have specific features in their light curves (their luminosity over time) that allows them to be classified. If a star falls into any of these types, we know that its variability is not due to the presence of an exoplanet.

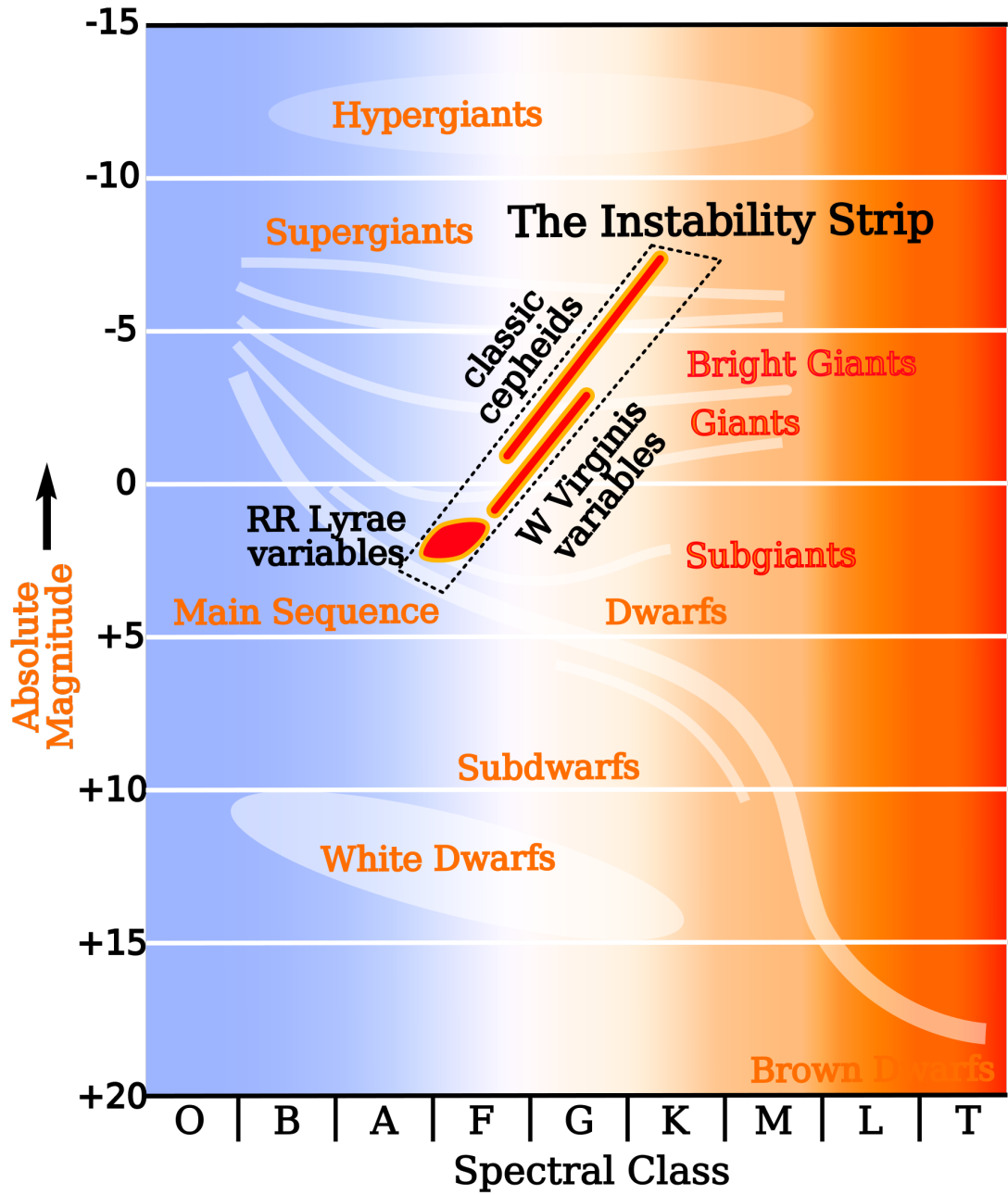


Figure 1.3: HR diagram with the instability strip included to show the region where intrinsic variable stars lie.

CHAPTER 1

1.2.1 Intrinsically Variable Stars

Stellar Pulsations

Stellar pulsations are caused by expansion and contraction in the outer layers of a star. Radiated energy from the core is trapped in the outer layers. This drives an increase in pressure which in turn causes the outer layer to expand. During the expansion the outer layer cools which then contracts under gravity. As stars seek to maintain hydrostatic equilibrium the changes in radii result in corresponding changes in the luminosity. This mechanism is classified by measuring the spectrum and observing the Doppler shift caused by the expansion and contraction (Koupelis, 2010). We do not have access to spectroscopy for our stellar sample, so cannot definitively classify all pulsation types, but stellar pulsations produce light curves (see Figure 1.4) which cannot be confused with those of exoplanet transits (see Figure 1.1).

Pulsations can be split into two groups, radial where the entire star expands and non-radial where different regions of the star expand and contract in different ways.

Cepheids

Classical Cepheid variables are Population I yellow supergiants (SG) which have variability periods between days and months. The variability of δ cephei was discovered in 1784 by John Goodricke. Henrietta Leavitt made extensive investigations of Cepheids early in the 20th century (Leavitt & Pickering, 1912). The light curves of Cepheids are periodic, with potentially large oscillations (upto ~ 1 mag), and which do not look anything like the signal from an exoplanet transit (compare Figures 1.1 and 1.4). In a classical Cepheid variable the luminosity is related to the period. The brighter the star the longer the period. Using the period we can calculate how bright the star should be and therefore work out how far away the star is. Type II Cepheid variables are Population II Stars, which have very regular light pulsations. They

CHAPTER 1

also have lower metallicity and lower mass compared to Type I Cepheids. Looking at Figure 1.3, Cepheids are found within the instability strip above the main sequence (MS) crossing through the Giant and Supergiant branches therefore Cepheids are predominately these two types. Type II Cepheid variables are also used as standard candles to determine extra-galactic distances (Majaess et al., 2009). However, Type II Cepheids can only be used to measure the distances to young galaxies with ongoing star formation. With dead older galaxies these Cepheids are no longer present.

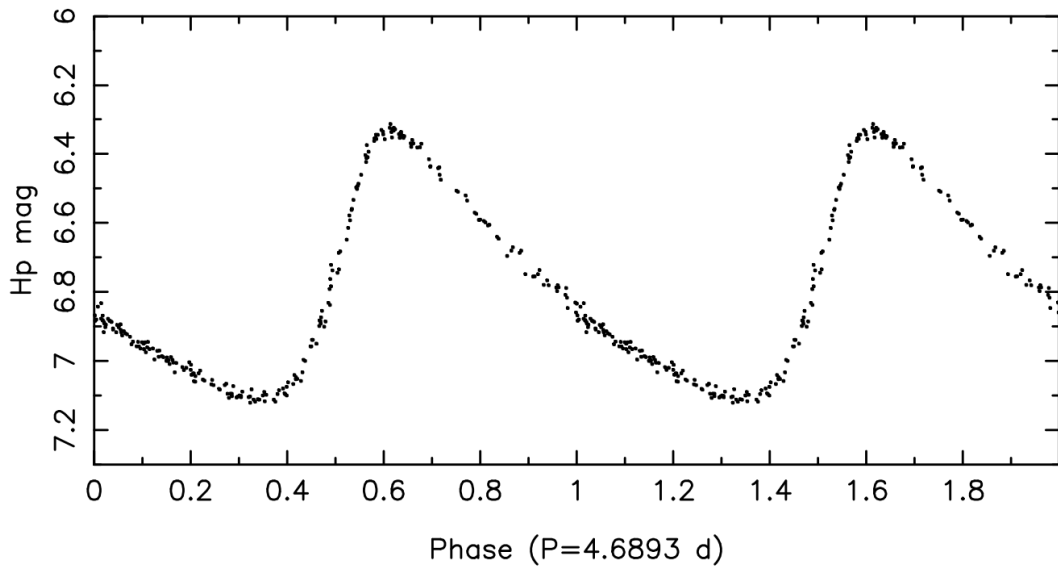


Figure 1.4: Hipparcos light curve of the classical Cepheid HD 112044 folded according to the oscillation period. Data taken from Perryman (1997, ESA).

Looking at Figure 1.4, we can see the characteristic saw-tooth shape of a Cepheid's light curve, with a steep increase in magnitude followed by a slower decrease in luminosity. This is a feature used as an identifier, along with the size of the change in magnitude.

CHAPTER 1

RR Lyrae

RR Lyrae stars are also Population II stars but have lower mass than Type II Cepheids. They vary in magnitude by 0.2 - 2 magnitudes. This is far larger in magnitude than exoplanet transits which typically cause dips of only a few 10s of milli-magnitudes. RR Lyraes are ageing pulsating horizontal branch stars of spectral class A or F. The relationship between the period and absolute magnitude of RR Lyraes allows them to be used as standard candles making them useful as distance indicators. They are also used in Globular Clusters (GCs) to look at the chemical properties of older stars. RR Lyrae variables do not follow a strict period-luminosity relationship at visual wavelengths, although they do in the infrared K band (Catelan et al., 2004). In Figure 1.3, RR Lyrae can be found just above the MS below the Cepheids and towards the lower end of the instability strip.

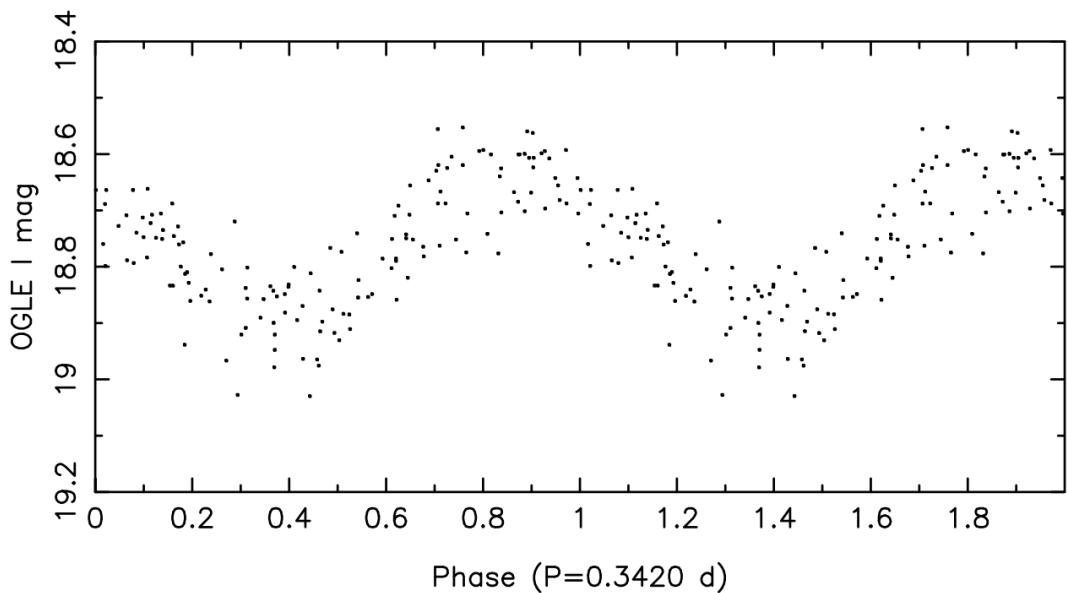


Figure 1.5: Light curve of an RR Lyrae star observed by OGLE folded according to the dominant oscillation period. (Aerts et al., 2010)

Figure 1.5 shows an example of an RR Lyrae light curve that has been folded onto itself, from which we can see that it does not resemble a light curve during an

CHAPTER 1

exoplanet transit. It also does not look similar to a Cepheid as it lacks the distinct saw-tooth shape. An RR Lyrae light curve is much smoother in both the rise and fall, approximating a sinusoid in shape.

RV Tauri

RV Tauri variables are variable stars which have a unique light curve with alternating deep and shallow minima. The magnitude amplitude can reach 3-4 V mag, with a period between 30-150 days.

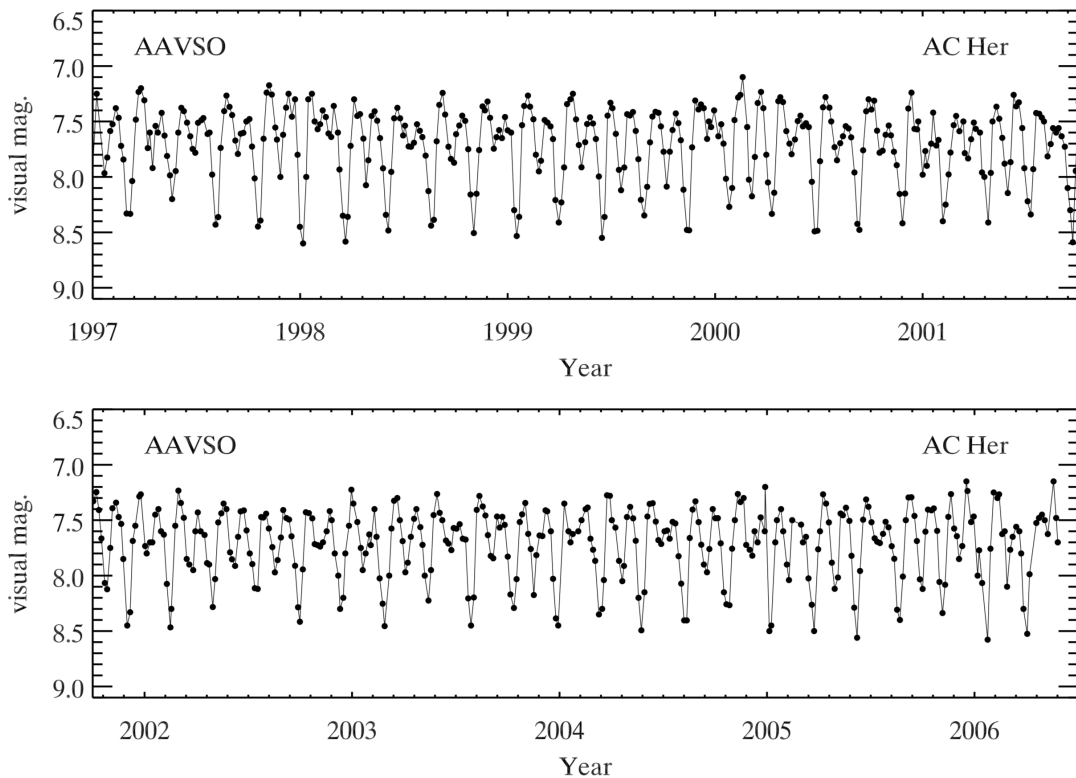


Figure 1.6: The visual light curve of the RV Tauri star AC Her as observed by the American Association of Variable Star Observers (AAVSO). Figure courtesy of Matthew Templeton. (Aerts et al., 2010)

In Figure 1.6 we can see that over nearly 10 years of observations that the light curve for this RV Tauri star follows a double wave pattern. The decrease as well as

CHAPTER 1

the increase in magnitude is also variable each time. The alternating deep and less deep minima is a characteristic used to classify variables as RV Tauri. The change in luminosity of a RV Tauri is related to radial pulsation on the star's surface.

Long Period Variables

Long-period variables are not strictly one type of star. However, the term does encapsulate Mira variables as long-period variables (Samus et al., 2009). Mira variables are named after the first prototype. Miras have a pulsation period longer than 100 days as seen in Figure 1.7 where the period of the illustrated star LX Cyg is ~ 1.5 years. This period is much longer than a Cepheid or RR Lyrae, and the shape is smooth and sinusoidal compared to that of a binary system.

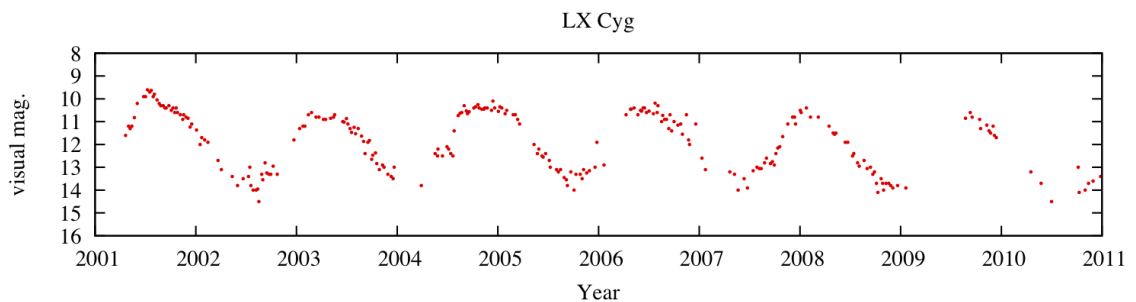


Figure 1.7: Visual magnitude light curve of LX Cyg observed over a 10 year span.

Eruptive/Cataclysmic Variables

Eruptive variables show extreme and rapid changes in luminosity, some examples are supernovae (SNe) and nova events. A nova occurs within a binary pair of a White Dwarf (WD) and another star either a main sequence, subgiant, or red giant star. A supernova (SN) is the end stage of a massive star as well as some less massive stars that evolve into WDs and subsequently accrete material from a companion. SNe are categorised into two main types, Type I and Type II. A Type Ia SN occurs when a WD within a binary system accretes enough mass from the donor star to approach the Chandrasekhar limit ($1.4 M_{\odot}$). As the WD reaches this limit it experiences

CHAPTER 1

a thermonuclear runaway reaction which leads to the SN explosion. The resulting light emission during such an event can be seen in Figure 1.8 as the green line. Type Ia SNe are important astrophysically as they can be used as standard candles due to the fact that they always occur to WDs of the same mass. Hence Type Ia can be used to determine the distances to galaxies. Type II SNe occur due to rapid collapse of a massive star ($8-40M_{\odot}$) (Gilmore, 2004). From Figure 1.8 the difference between Type I and II can be seen, both types have a very rapid increase in luminosity which slowly fades away, however the rate at which they fade is dependent on type.

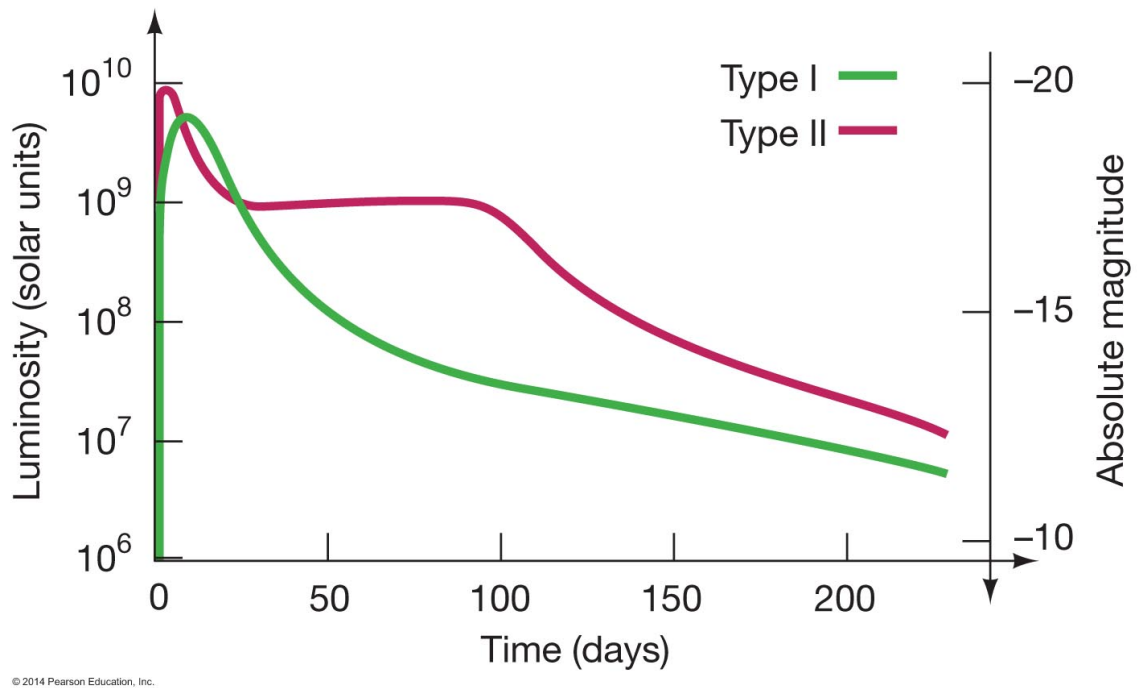


Figure 1.8: Graphic representation between a Type Ia and Type II SN (Brau, 2019).

As catastrophic, usually one-off (some Novae recur) events, novae/SN produce light curves that cannot be mistaken for planetary transits (Figure 1.8). For novae events that do reoccur the time scale for these is $\sim 10-80$ years, far longer than the timescale of MOSES observations.

Eruptive variable stars vary in brightness due to violent events such as flares, which

CHAPTER 1

occur on the surface of the star. These flares occur due to charged particles interacting with the plasma medium, with magnetic reconnecting leading to large amounts of accelerated charged particles (Zhu et al., 2016). Not all flare events are the same and each have their own unique light curve, none of which look like an exoplanet.

1.2.2 Extrinsically Variable Stars

Eclipsing Binaries

Eclipsing binaries (EBs) are binary star systems where the the orbital plane of the system roughly lies on the line of sight of the observer so that each star undergoes mutual eclipses (Bruton & Stephen, 2007). EBs are variable stars due to the eclipses that occur, not because of the light from either or both stars is varying. In effect they are a more extreme version of the situation for transiting exoplanets. The light curve of an EB is characterised by a period of constant light with periodic drops in intensity as the stars pass in front of one another. If one star is considerably more luminous and much more extended than the other, eclipsing binaries can produce light curves similar to those of transiting exoplanets. To determine the difference between a binary system and an exoplanet we look at the light curves of each. When looking at the light curve of a binary system we notice that there are two dips of unequal depth, as shown in Figure 1.9. We know this shape is not due to a transiting planet. If it were a planet, there would only be one significant dip against a constant luminosity, a second dip is technically there but is not practical to observe, as shown in Figure 1.1.

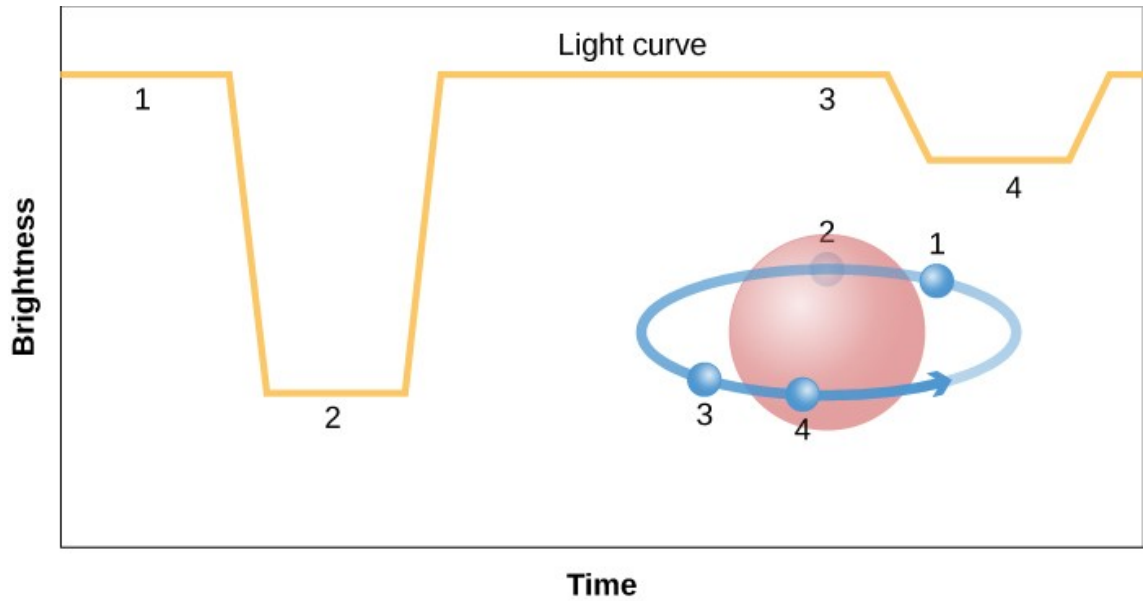


Figure 1.9: A graphic representation of a binary system's light curve (ER Services, 2018).

1.3 Moving Objects

As well as the variable stars and exoplanets we have also seen moving objects within our survey field. A near-Earth object (NEO) is a small object within our solar system whose orbit brings them within close proximity of the Earth. For an object to be classified as a NEO it must pass within 1.3 AU of the Sun (Chodas et al., 2019). The majority of NEOs are asteroids but a small number are comets. When a NEO is observed there are no clear dips in luminosity comparable to that of an eclipsing binary or an exoplanet, the object simply moves across the sky over time, ruling out any object outside the solar system.

Chapter 2

Existing/Previous Exoplanet Surveys

This Chapter will briefly discuss recent survey projects that have searched for exoplanets and variability to provide some context for the MHT Optical Star and Exoplanet Survey (MOSES) survey. The two Kepler missions were a huge step forward in the search for exoplanets as the first space telescope dedicated for this purpose (Borucki et al., 2003) with TESS becoming the successor space mission (Ricker & TESS Team, 2015). Besides space missions there are still ground based surveys continuing the hunt for variability such as the WASP and Evryscope projects (Pollacco et al., 2006) (Ratzloff et al., 2019b).

2.1 The Kepler Mission

The Kepler spacecraft was launched on 2009 March 6 from NASA's Cape Canaveral Air Force Station. The original mission for the telescope was to monitor 150,000 main-sequence (MS) stars for planets, with the mission to last for 3.5 years with possible extension for another six years (Johnson and Dunbar, 2018). The mission

CHAPTER 2

was specifically designed to survey our Milky Way (MW) galaxy in search of exoplanets that lie close to the habitable zone and therefore to find the number of stars within the MW which could have habitable planets. The original mission came to an end in August 2013 after two of the guiding gyroscopes failed.

2.1.1 K2 Mission

In 2014 a second mission commenced for the spacecraft called the *K2* mission (Howell et al., 2014). The Kepler spacecraft was finally retired in November 2018. During the two missions, Kepler observed a total of 530,506 stars (Chen, 2018), with 3873 (NASA Exoplanet Institute, 2019) confirmed exoplanets and many more probable exoplanets. As previously mentioned not all of the exoplanets can be confirmed by the Kepler mission due to the lack of repeated observations of transits. Hence one reason why ground-based surveys are useful, is that they allow observations over longer temporal baselines and at a lower cost. A ground based survey allows for a longer baseline with the cost of a worse observational cadence compared to a space mission. The cadence of a ground based survey is firstly limited to night time, it is then subject to weather conditions, as adverse weather such as rain, clouds and heavy wind will prevent observations.

2.2 The WASP Project

The WASP project was designed to search for bright transiting exoplanets which would be suitable for spectroscopy at a later date. The SuperWASP Cameras are wide-field imaging systems sited at the Observatorio del Roque de los Muchachos on the island of La Palma in the Canary Islands, and the Sutherland Station of the South African Astronomical Observatory (Pollacco et al., 2006). The WASP system used eight telephoto camera lenses in a 4x2 array each with a CCD attached.

CHAPTER 2

The CCDs consisted of 2048 x 2048 pixels, 13.5 μm in size. Both of the WASP instruments had a 482 deg² field of view, able to survey the entire visible sky every 40 minutes. During the first 6 months of the northern observations ~ 6.7 million objects were detected.

Although WASP found many objects it was relatively limited in what it could detect, as the WASP cameras have an angular scale of 13.7 arcsec pixel⁻¹ leading to significant problems with stellar crowding for fainter objects. The collecting area of the lenses are small meaning only the brightest (7.0-11.5 V mag) stars could be observed. However, the Moses Holden Telescope (MHT) has an angular scale of 1.18 arcsec pixel⁻¹ allowing closer objects to be resolved even when considering the typical seeing at Alston of ~ 3.5 arcsec. The MHT is also able to see fainter objects than WASP due to its much larger collecting area (70cm diameter telescope). The WASP camera had an effective range of V ~ 7.0 to 11.5 but with lower quality data can detect objects up to V ~ 15 (Pollacco et al., 2006). The MHT is able to examine objects from $\sim 11 - 17$ V mag in a 60 s exposure, therefore allowing us to detect objects missed previously by the WASP survey.

2.3 Evryscope

The Evryscope is telescope array designed to look at a very large area of sky to detect short timescale variability. The array is comprised of a 780 Mega pixel 22 camera array with a 8150 sq. degree field of view, 13 arcsec per pixel (Ratzloff et al., 2019b). The telescope has a 2 minute cadence for observations with around 5000 images per night with $\sim 300,000$ sources per image (Ratzloff et al., 2019b). The Evryscope is located in Chile.

Using the multi-year Evryscope data Ratzloff et al. (2019a) searched for high-amplitude variable objects from 160,000 stars brighter than 14.5 V mag. In this study Ratzloff et al. (2019a) searched the stars that are both 9 - 14.5 V mag with

CHAPTER 2

declinations -75° to -90° . They recovered 346 known variables and discovered 303 new variables, including 168 eclipsing binaries. However, with the Evryscope located in Chile, it is only possible to survey the southern hemisphere sky. Therefore the Evryscope is unable to observe the same objects as the MHT as it cannot look at the northern sky and the MOSES survey field.

2.4 TESS

On the 18th April 2018 the Transiting Exoplanet Survey Satellite (TESS) was launched aboard a SpaceX Falcon 9 rocket (Ricker & TESS Team, 2015). Unlike Kepler which only surveyed a small region of the northern hemisphere sky, TESS will survey the entire sky (400 times larger than Kepler) starting with the southern sky then moving to the northern sky taking a total of two years looking at the brightest 200,000 stars at a 30 minute cadence. In order for TESS to survey the entire sky it will be broken down into 26 sectors, each 24 degrees by 96 degrees across, each sector will be observed for a minimum of 27 days (Ricker & TESS Team, 2015). With this observing strategy TESS is ideally suited to look for short transit period exoplanets. Due to TESS changing sector every 27 days it will be very difficult to detect exoplanets with periods >27 days, as TESS cycles through each sector it would therefore be difficult to observe multiple transits. The first light image from TESS was taken on August 7, 2018, and released publicly on September 17, 2018 (Kazmierczak & Garner, 2019). As of August 2019 TESS has confirmed 28 new exoplanets. Recently the TESS project has announced that it will no longer be surveying in the same region as the MOSES survey. Therefore candidate objects found with MOSES will no longer be observed by TESS.

Chapter 3

MOSES Project Hardware

3.1 The Moses Holden Telescope

The Moses Holden Telescope (MHT) is a Planewave CDK700 telescope upon an Alt-Az mount. The MHT is located at Alston Observatory (+53.80°N, -2.59°W), with registration with the Minor Planet Centre (registered number Z49). The MHT has a 0.7 m primary mirror, with an 83% effective collecting area. The MHT has a secondary mirror of 0.29 m and a tertiary flat mirror used to reflect the light either to the CCD or eyepiece. The full light path for the MHT can be seen in Figure 3.1.

With the addition of a focal reducer the MHT has a 40 x 40 arcminute field of view. The MHT and CCD now has a pixel scale of 1.18 arcsec/px. The typical seeing at Alston Observatory is ~ 3 arcsec and therefore the MHT observes 3 pixels to an objects FWHM, greater than the 2 pixel required for nyquist sampling. The Alt-Az mount used has a pointing accuracy of 2 arcseconds with a tracking accuracy of < 1 arcsecond over a 10 minute period and field de-rotation accuracy of 3 microns of peak to peak error at 35mm off-axis over 1 hour of tracking (18 arcsec) (Planewave Instrument, 2019).

With its large field of view and relatively large collecting area the MHT provides an ideal tool to undertake an imaging survey.

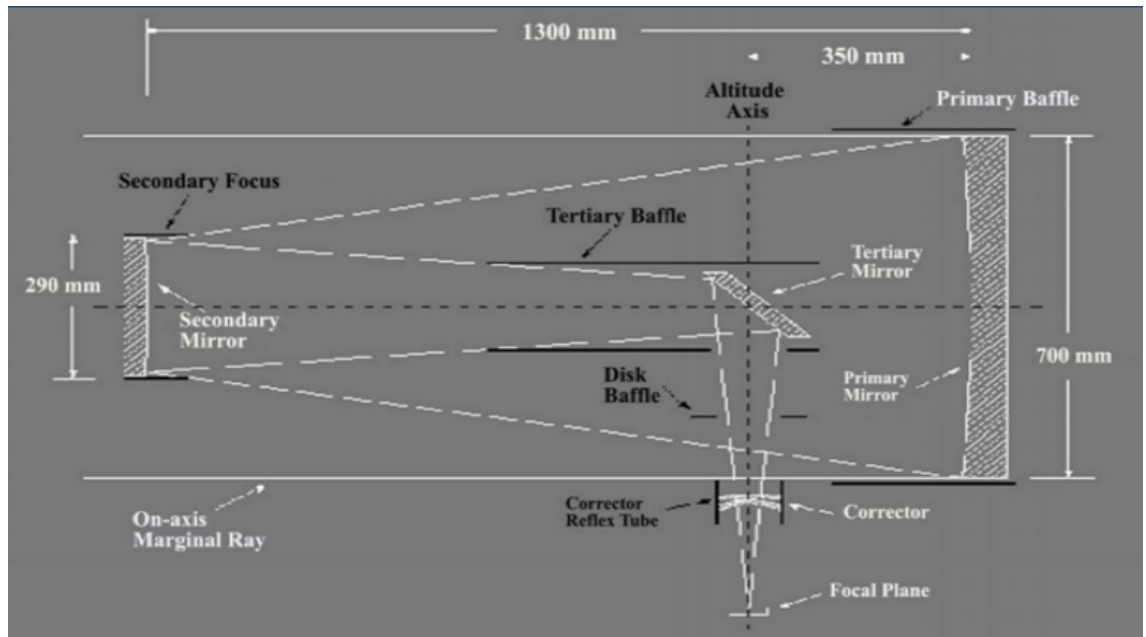


Figure 3.1: Schematic drawing of the Moses Holden Telescope (Star.uclan.ac.uk, 2018)

3.2 The CCD & Filter Set

The MHT is equipped with an Apogee Aspen CG16m CCD. The CCD itself is a 16.8 Megapixel sensor with 16-Bit digitisation consisting of 4096×4096 pixels, each $9 \mu\text{m}$ in size. The MHT has a native plate scale of $\sim 45 \text{ arcsec } \text{mm}^{-1}$. The CCD is capable of operating 60°C below ambient using cooling to maintain CCD temperature. For our observations the temperature of the CCD was set to -35°C providing a compromise between cold and warm weather operation, as with warmer weather the cooling would fail to reach a lower setpoint. The MHT is equipped with the Johnson-Cousins filter set (Star.uclan.ac.uk, 2018). The filter set is comprised of five different wavelength bands U, B, V, R & I. Our observation used the V band exclusively, with a central wavelength of 545 nm (Karttunen et al., 2007). As well as being in part of the visible spectrum this wavelength also falls in the highest

CHAPTER 3

quantum efficiency range for the CCD of 500-600 nm, as shown in Figure 3.2 from the Apogee handbook.

Quantum Efficiency (QE) Curve^{*4}

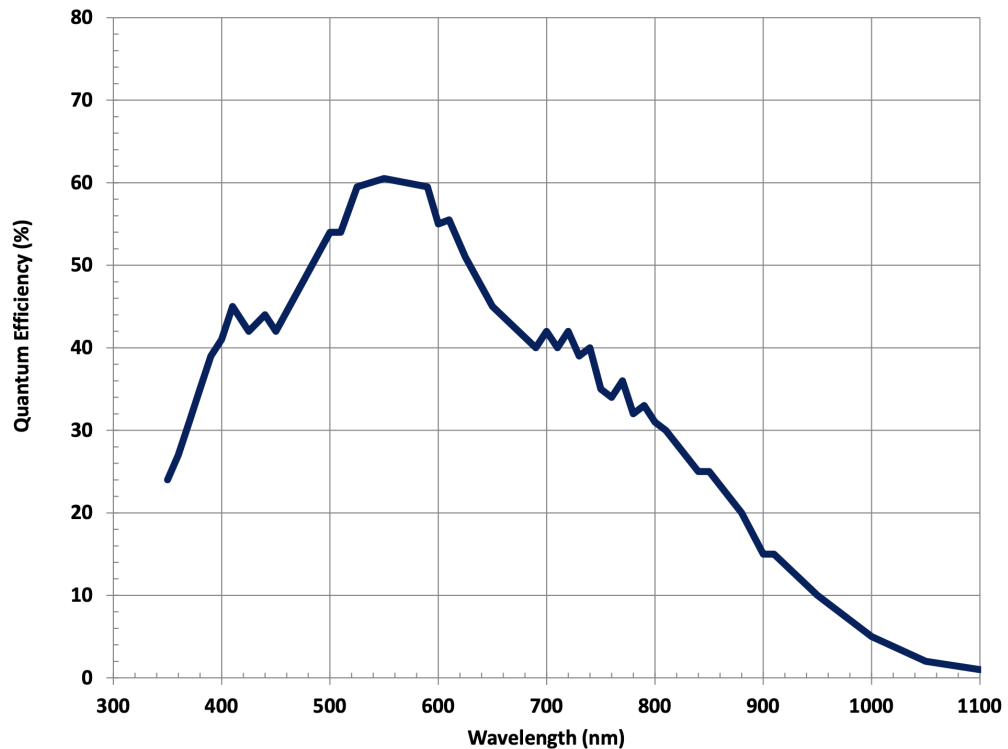


Figure 3.2: Quantum efficiency graph for the CCD equipped to the MHT (ANDOR, 2019).

3.3 Software

The MHT utilises two software packages for operation. The telescope's movement is controlled by Planewave software (Planewave Software, 2019), this allows the target survey field to be selected and tracked through the night. This software also automatically tracks the rotation of the sky setting the de-rotation angle needed for each individual image of the mosaic. The filter wheel operation and imaging of

CHAPTER 3

the CCD is controlled by MAXIM DL6 (Diffraction Limited, 2019). This software is used to set the size and dimensions of mosaic used for the survey field. The exposure time for each tile of the mosaic is also set as well the filter used for the exposure. It also controls the dithering and offsetting for the mosaic.

Chapter 4

Observations

4.1 Analysis of Exoplanet Archive Data

To aid in our selection of survey field and observation strategy we looked at the NASA Exoplanet Archive (Johnson & Dunbar, 2018). The archive data for all confirmed exoplanets was downloaded to be examined. As the practical observing season at Alston Observatory is ~ 6 months long, we wanted to know the distribution of known exoplanets that have a period of less than 6 months as more than one transit dip is required to be confident of a positive detection. Exoplanets with periods longer than 6 months would not be detectable to us or at least confirmable, in a single observing season. Figure 4.1 shows the distribution of periods for known exoplanets, from this we can see that $>90\%$ of known exoplanets have a period <100 days. This value is likely to be heavily affected by selection effects, as long period exoplanets are more difficult to detect requiring very long duration observing campaigns and are in fact impossible to detect in short surveys. As well as the period, the transit duration is also an important factor to consider when constructing an observing strategy. From Figure 4.1 we can see that 80% of exoplanets have a transit duration less than 12 hours. For our observations the maximum observation hours per night is ~ 12 hours. Very few exoplanets have periods shorter than 12 hours.

CHAPTER 4

Therefore, we would be typically able to observe a single transit within a single night's observations. Though of course long duration eclipses can be detected even if only part of the eclipse occurs during an observing night (with very short transit durations it is likely to miss a transit as we point at the other pointings of the survey mosaic if the mosaic is too large). The exposure time and number of pointings within the mosaic is therefore set by the typical duration of a transit. We want to ensure that for a typical transit duration we would obtain >5 exposures during the dip, as a single observation would not be convincing given typical photometric uncertainties.

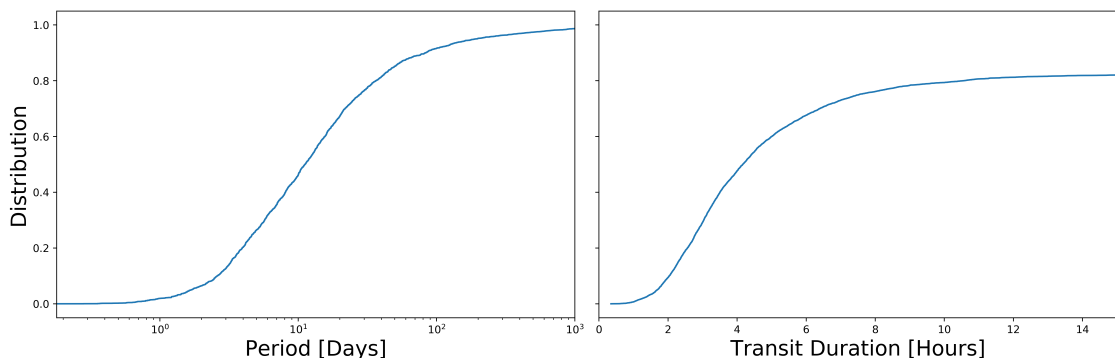


Figure 4.1: Left Panel: Cumulative Distribution for known exoplanet periods with the Period limited to <180 days. Right Panel: Cumulative Distribution for known exoplanet transit with the Transit Period limited to <15 hours. (Data from (NASA Exoplanet Institute, https://exoplanetarchive.ipac.caltech.edu/docs/counts_detail.html, 2019))

4.2 Survey Field Selection

The survey field chosen is centred around R.A. 2h 18m 17s, Dec $63^\circ 30' 44''$ seen in Figure 4.2. This location was chosen as it met the following criteria: The location is situated in a spiral arm of the MW with a high stellar density providing many targets. The field is visible for our whole observation season which runs from October to April, as the field is above a Declination of 60° placing it in the continuous viewing

CHAPTER 4

zone for the MHT. The field also had to avoid any very bright $V < 6$ magnitude stars, as stars of this brightness and brighter would create reflections, glints and saturate the CCD which would limit the effectiveness of aperture photometry in adjacent areas. Finally the stellar density is not too high, otherwise stellar crowding would limit photometric accuracy.

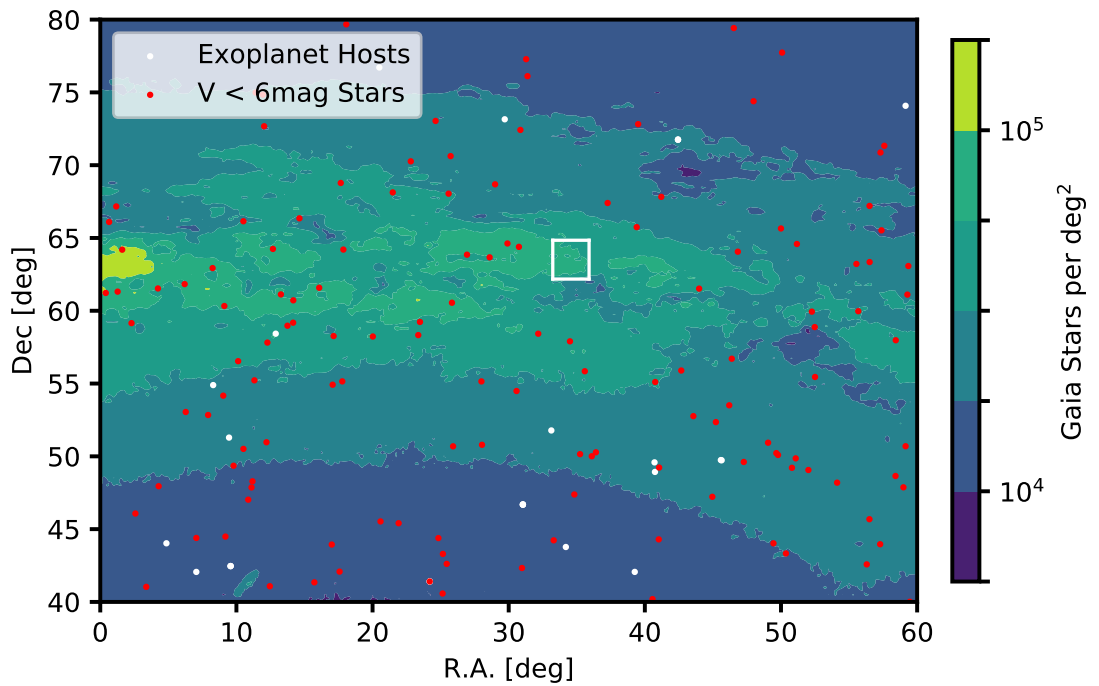


Figure 4.2: This Figure shows the MOSES field indicated as the white square (~ 7 square degrees). The red points are bright stars ($V < 6$ mag) to be avoided due to CCD saturation, the white points are known exoplanet host stars and the colour map shows the density of Gaia stars across the sky. (UCAC4 catalogue data used to find $V < 6$ mag stars. The Gaia stellar densities were obtained from gaia.ari.uni-heidelberg.uni.)

4.3 Observing Strategy

To sample the field a 4 x 4 mosaic centred on the chosen field centre was used. Hence 16 images were observed in sequence and were given a mosaic co-ordinate position. This co-ordinate position is added to the file name automatically by MAXIM DL6 to easily identify where each image is positioned within the survey field. The order of observations and the tile positions can be seen in Figure 4.3. The duration of the mosaic sequence is controlled within the MAXIM DL6 software. Within the software the exposure time for each image can be set and a delay between each image is set to allow the telescope to settle after each slew between tiles. Each image had an exposure time of 60s which allows us to obtain photometry for objects with magnitude between $11.5 \leq V \leq 17$ mag. To capture each full mosaic it takes around 23 min. This allows a 1hr transit to be observed 4 times. 99.3% of known exoplanets have a transit duration ≥ 1 hour. A 5x5 mosaic takes >40 minutes to complete and be reset, greatly reducing the number of epochs per object. This process was repeated throughout the night allowing for a maximum of 25 visits of each pointing per full night. In between each mosaic the telescope had to be manually reset to the initial starting location. Each image from the MHT is 40 x 40 arcmins; this makes the full FOV of the mosaic ~ 7 square degrees. Based on our first night of observations we found the signal to noise ratio at magnitude $V=12$ is 384 and at the lower limit of $V=17$ signal to noise is around 5 (See Figure 4.4). Therefore, our working magnitude range will be 11.5 - 17 V mag.

CHAPTER 4

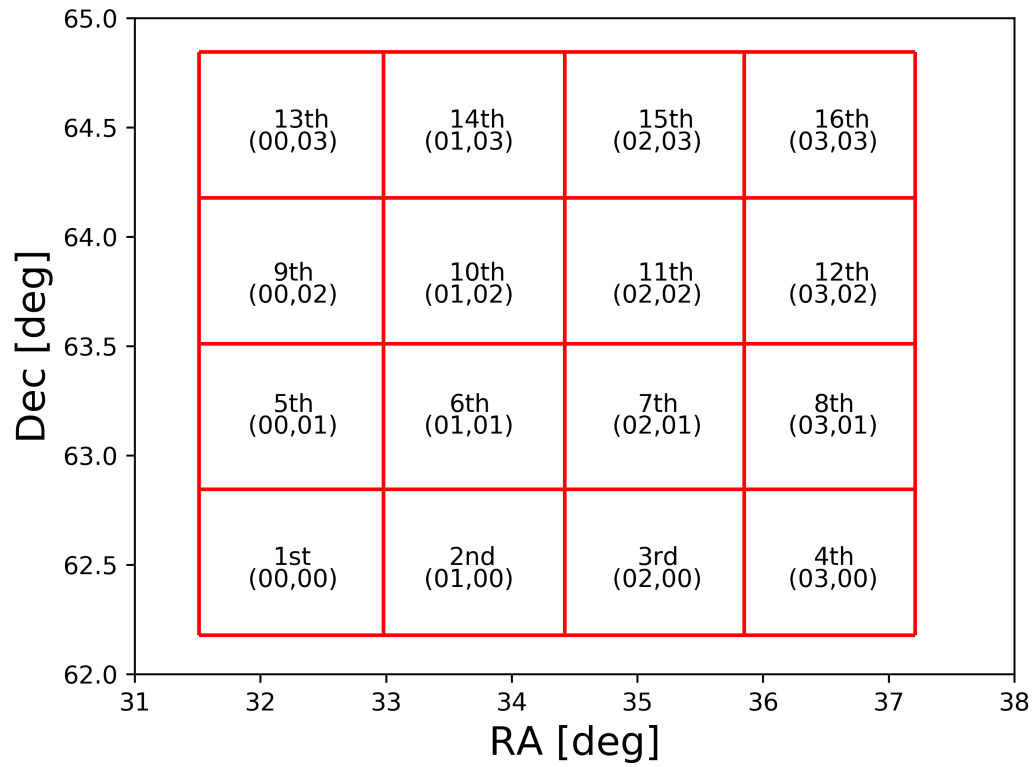


Figure 4.3: Mosaic tile positions used with the image sequence order and tile location indicated on each tile.

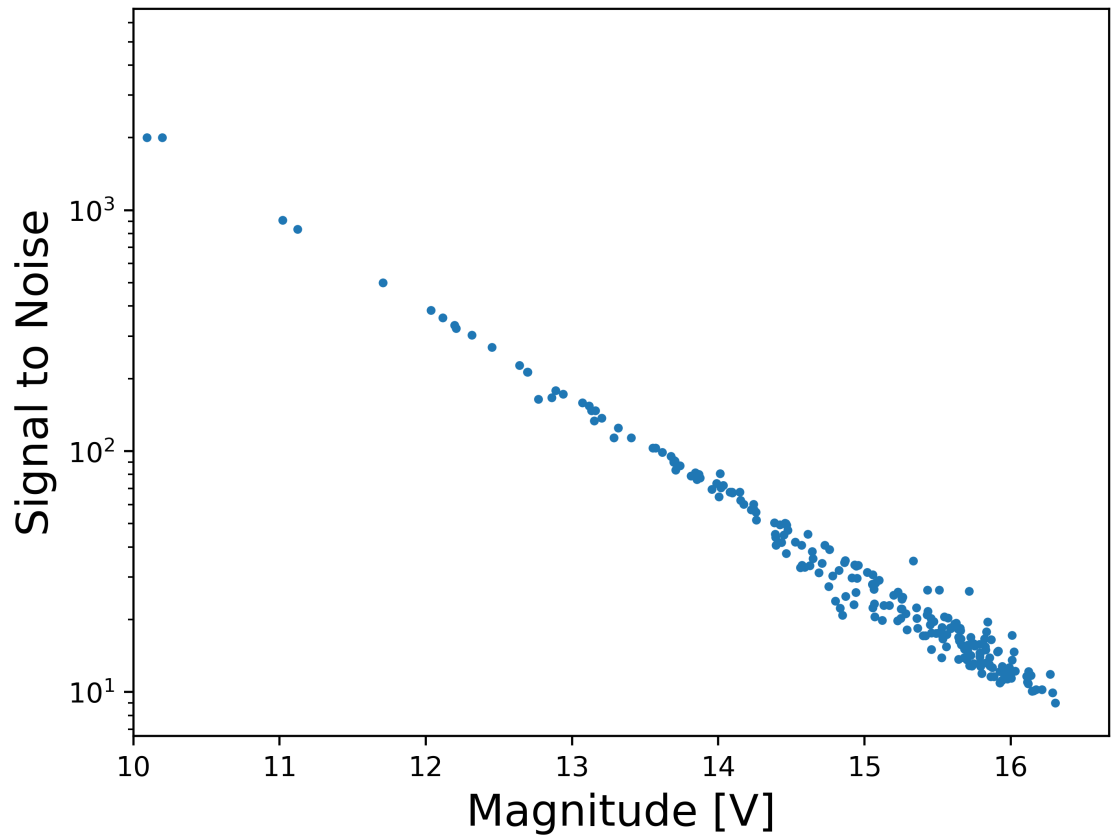


Figure 4.4: Signal to noise ratio vs magnitude as measured for early test observations of duration 60s. S/N will depend on transparency and seeing, but these values are representative of typical values for the survey.

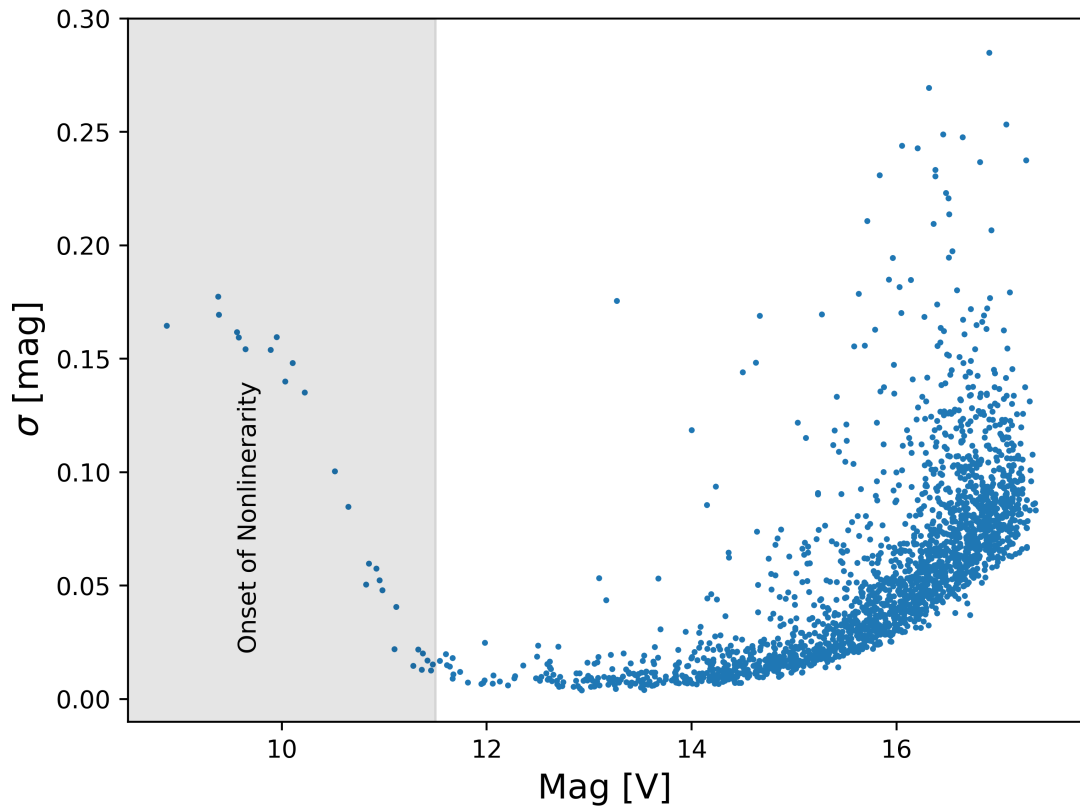


Figure 4.5: Standard deviation of magnitudes for objects initially observed with a 60s exposure.

Figure 4.5 shows the the magnitude for each object against the standard deviation in magnitude. The standard deviation is calculated from the magnitude range over the total number of observations during the survey for each object separately. There is a noticeable increase in the spread in magnitude for object brighter than 11.5 V mag. This is due to the onset of non-linearity which happens when the very high number of photons is incorrectly counted by the CCD. The effect occurs when a pixel within the CCD approaches being full the electrons within the pixel begin to repel additional charge. Therefore, as the pixel fills up with charge the luminosity to electron relation is no longer linear. Any objects that are much brighter than 11 V mag would saturate the CCD within a 60s exposure. Therefore these objects

CHAPTER 4

will have an inconsistent and inaccurate measurement with aperture photometry as their photometry will depend strongly on the seeing during the observation.

From our first night of observing we saw just over 34,000 stars, however, the seeing conditions were not ideal. Therefore, over the course of the first season we have seen >87,000 objects. The signal to noise for the objects first detected had a ratio at magnitude $V=12$ is 384 and at the lower limit of $V=17$ signal to noise is around 5. As Kepler detected planets around $\sim 1\%$ of its target stars we predict an upper limit of ~ 500 exoplanets for our survey.

4.4 The Reduction Pipeline

To reduce the images from the MHT a Python script has been written. Python was chosen to utilise existing libraries `astropy` and `ccdproc`. These two libraries are used to perform the reduction process. The script opens a directory where the most recent calibration images are stored. A master dark frame is created by combining all the most recent dark images together using `ccdproc.combine` set to calculate the median. This is the same method used to create the master bias frame. To create the master sky flat frame a similar method to the bias frame is used with the additional step scaling the images to account for varying sky brightness. Each of the three master calibration frames is saved to be used for image reduction. Each science image is reduced in turn, the dark subtraction is performed first on the image followed by the flat field correction, as dark images contain the bias a separate bias subtraction is not required. For the science frames the bias frames are used exclusively in the production of the flats. The final step in the reduction script is the correction of the world co-ordinate system (WCS) (described in detail in section 4.4.2). Once each image had been through the astrometric correction it was given a unique name based on the mosaic tile position and the HJD of the observation and moved to a storage directory.

4.4.1 Calibration Frames

Bias, dark and twilight flat frames were taken as frequently as possible. Due to weather conditions it was not possible to obtain twilight flat frames for each observing night, therefore flats obtained closest in time to a night's observing were used. This is done to reduce the effects of variation in flat efficiency over time.

4.4.2 Astrometry

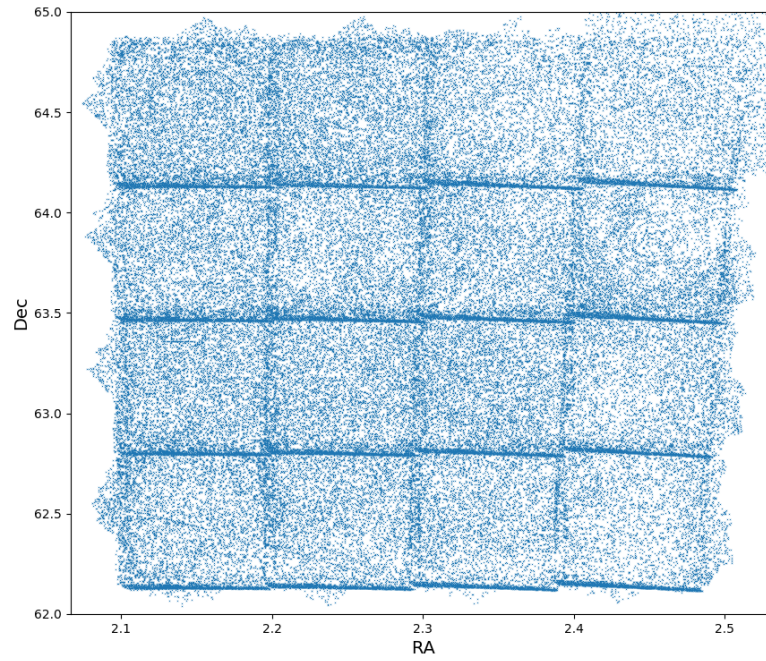
Due to the MHT having an unusually wide FOV (40x40 arcmin) barrel distortion (projection of a curved focal plane onto a flat CCD) becomes noticeable towards the corners of the frame. As each image is taken and saved the automated world co-ordinate system (WCS) fit which is saved to the FITS header is inaccurate in the edges and corners of the image (~ 8 arcsec of distortion). To fix this we used Astrometry.net running within a Python script to solve and produce a new WCS that would be used in creating our catalogues. An online version of this software is also available but can only correct a single image at a time, therefore it was necessary to create a scripted procedure to speed up the process. Astrometry.net uses the cleaned USNO-B Catalogue (Astrometry.net, 2019) to obtain an accurate position for each object within the image. It works by comparing the MHT image to a catalogue of star positions and magnitudes. A correction precision of ~ 2 arcsec is required for our catalogue process to ensure stars are correctly analysed. To achieve the 2 arcsec precision in the corner and edge regions a 5th polynomial fit was used as this gave the required correction level, higher order fits also achieve these correction results but take significantly longer to process with diminishing returns.

4.5 Post-reduction Calibration

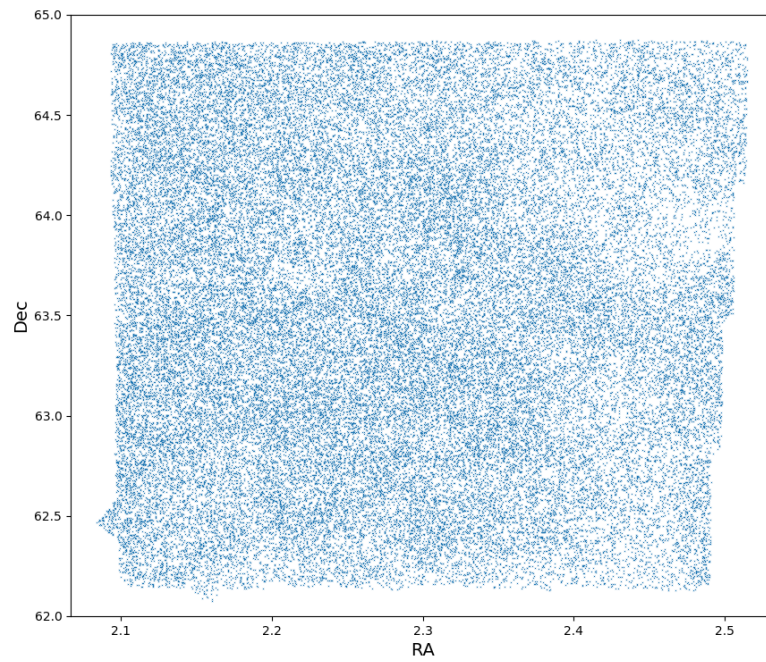
4.5.1 Border Pixel Removal

To test the astrometry correction the position of each object was plotted. In Figure 4.6a, all detected objects have been plotted even if only detected in a single image. From the plot we can see there is a high number of apparent objects along the edges of the CCD. This is due to the CCD having a high number of artefacts close to the chip edge, which appear as genuine objects but in fact are bad pixels. In Figure 4.6b, a 12 arcsec (10pix) crop has been carried out ignoring any object found within this CCD border region. With this crop in place the number of false detections is dramatically reduced. From Figure 4.6 we can also see that on specific occasions the de-rotator of the telescope had failed during a single observation or the pointing was in error leading to a number of objects occasionally detected outside of the fiducial survey field.

CHAPTER 4



(a) Object positions without 10 pixel crop.



(b) Object positions with 10 pixel crop.

Figure 4.6

4.5.2 Vignette Correction

The images taken using the MHT have a noticeable vignette towards the four corners. This creates the issue that objects detected towards these regions appear to be fainter than they are in reality. This was not fully corrected for in our image reduction process, the flat fielding did not fully remove this effect, therefore additional procedures had to be undertaken. In order to correct this we used the UCAC4 Catalogue to obtain absolute magnitudes for objects within each image. Using the magnitudes from the UCAC4 Catalogue we are able to perform an initial zero-pointing. From Figure 4.7 we see the zero-pointing is not accurate across the entire image. Objects in the corners are fainter by ~ 0.04 V mag. Using the magnitude delta of the objects from the UCAC4 Catalogue within our image we can interpolate the magnitude correction needed at any point on the CCD. This correction value is then used to amend the photometry for each object within this image. This process was incorporated into our catalogue script. As well as the zero-pointing including a vignette correction we use a second method of differential photometry when examining for variability. However, we still make use of this relatively crude zero-pointing as it gives us a reasonable representation of the object's average magnitude as seen in the sky.

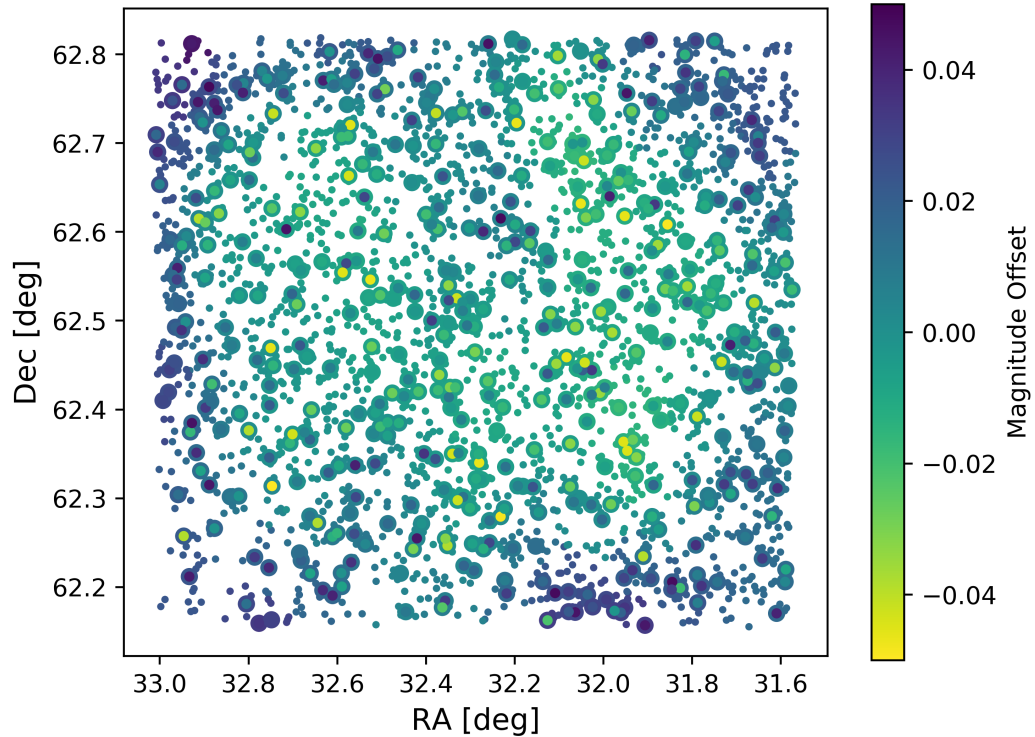


Figure 4.7: Objects within the image are plotted as single points. Objects that are found within the UCAC4 Catalogue have an additional ring around the point. The colour scale is V Magnitude offset between Catalogue and measured magnitude.

4.5.3 Differential Photometry

In addition to the post reduction calibration a further step of differential photometry has been applied. A list of differential photometry stars has been created for each individual tile of the mosaic. This ensures that the differential photometry star used is observed within the same frame as the object star for all observations. For a star to be a differential photometry star it needed to be visible in $>90\%$ of observations per mosaic tile. The star also had to be a non-variable. To determine this the standard deviation of each differential star had to be $<1\sigma$ V mag. The star also had

CHAPTER 4

to have a V magnitude between 11-14.5 V mag and be within ~ 5 arcmins of the object star.

We use differential photometry when searching for variability within our objects. The photometric values used with this method are better when searching for variability. This method provides better results as it is localised as the separation between object star and differential star is < 5 arcmins. The differential photometry are also carried out for each frame individually which will also take into account for situation where there maybe cloud passing over a section of the observation. It also accounts for the seeing conditions at the time of exposure.

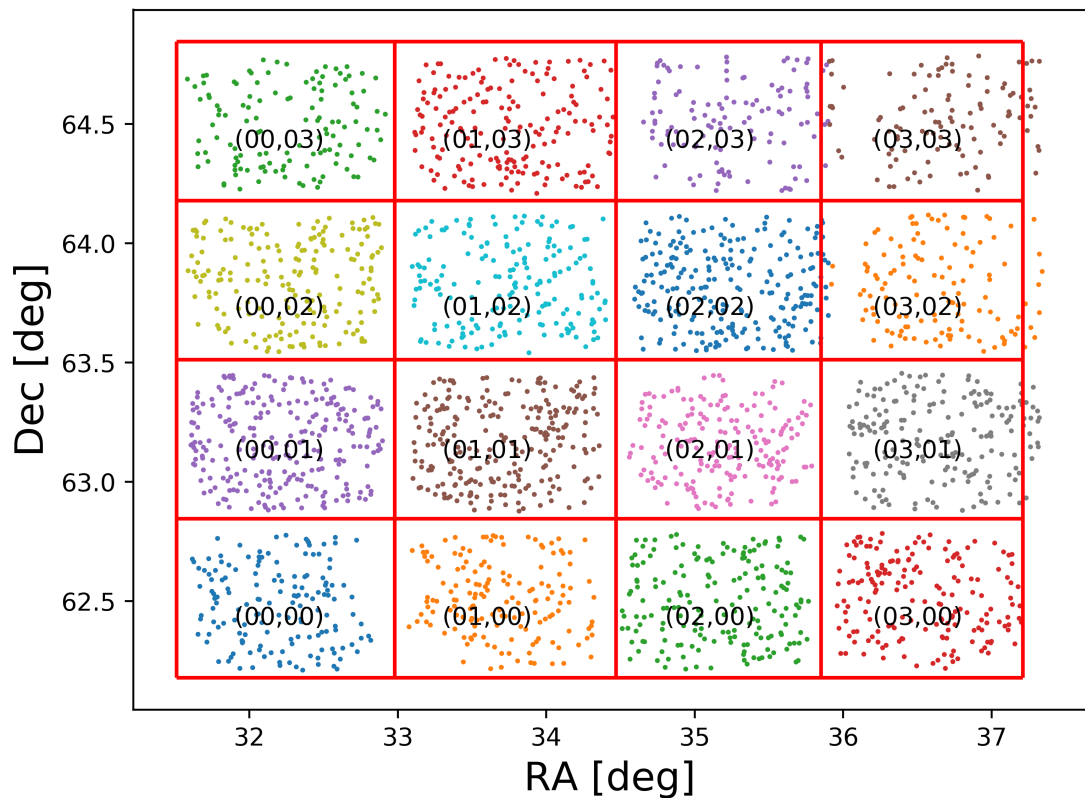


Figure 4.8: The location of each differential photometry star selected specific to each tile.

When an object is detected the distances to the list of differential photometry

CHAPTER 4

stars is calculated and the closest differential photometry star to the object star is located within the current image being processed. The magnitudes for the differential photometry star are then added to the object star's data file to be used for the differential photometry at a later stage. Each of the separate sets of differential photometry stars can be seen in Figure 4.8.

Chapter 5

The Catalogue

5.1 Aperture Photometry

To create the Master Catalogue, SExtractor (Bertin & Arnouts, 1996) was run using the python wrapper `sewpy`. This allows us to incorporate the vignette correction into one script. With source extractor we are able to pull out the specific data we required to create the Master Catalogue. The script is run for the first time on a single image and each object detected has its observation date and position stored into the Master Catalogue data file (see Table A.2 in the Appendix for an excerpt of the Master Catalogue). Each object detected also has a unique data file created which logs the JD, position and photometry (see Table A.3 for an example of the data stored for each object detected). The script is then run again now looking for objects observed multiple times. Each image within the storage directory is read in by the script which will then perform the aperture photometry on every object. The output from the source extraction is temporarily stored until written to an object file. The objects detected have to be checked against the Master Catalogue to determine if an object is new or had been observed before. The Master Catalogue is read in and each object is compared in turn to the Master Catalogue using `SkyCoord`. We set a positive match to be an object within 2 arcsec of its first observational position.

CHAPTER 5

A 2 arcsec separation is well matched to the typical seeing of 3 arcsec, therefore any objects closer than 2 arcsec would be difficult to distinguish anyway. If two new objects are within the 2 arcsec radius of a previously detected object then the closest new object is set to be the same object. Once the positive match is made the object data file is opened and the new data of JD, position and photometry is appended to the file along with the zero point star data. This process is continued for all of the objects within the new image. If a new object is detected for the first time the object's observation date and position is then added to the Master Catalogue and a new unique object file is created. This process is allowed to run on all the images within our storage directory. After all images have been processed through the Catalogue script the Master Catalogue is now complete with every object detected having its own data file. Using this procedure we have detected 87,397 unique objects, including 29,399 objects with >200 measurements.

5.2 Previously Detected Variables

Using the SIMBAD Astronomical Database (Wenger et al., 2000) to check for any known variables within our survey, we find two variables, RAFGL 315S and TYC 4037-209-1. These are the only two known variables within the MOSES survey field. Using the SIMBAD co-ordinates we are able to locate the variable stars in our Master Catalogue. For RAFGL 315S, we produced a light curve from the specific object data file as it has a single period to compare our plot against.

From Figure 5.1 we confirm our ability to detect variable objects within our data set. We have also estimated a period of 120 days as a first approximation before a Fourier analysis using Period04 (Lenz & Breger, 2005). The star also has spectral type M5. From this information we would therefore classify this star as a likely Mira type variable.

CHAPTER 5

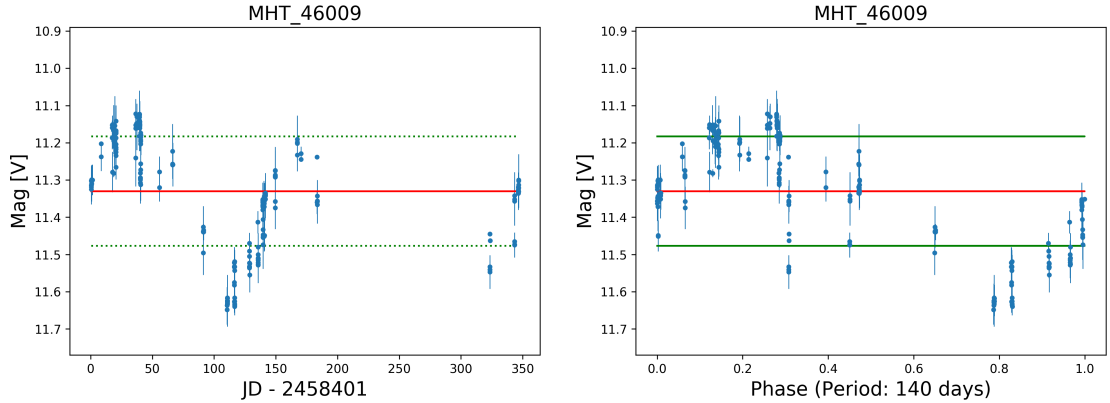


Figure 5.1: Light curve of variable star RAFGL 315S, with local Catalogue number MHT 46009. The right panel of the folder light curve using a calculated period of 140 days. The red line indicates the median V mag, with the green line the standard deviation above and below the median V mag.

5.3 Data Cut

For our analysis of the data we have chosen to examine in detail a more restricted sample. We have $>84,000$ light curves which is simply too large of a data set to analyse in detail for this thesis. We have made therefore three cuts to the data. The first cut (vertical red line in Figure 5.2) excludes any object with a mean magnitude brighter than 11.5 V mag, as objects this bright will have saturated the CCD and therefore do not have reliable photometry (as explained in Section 4.3). The second cut (horizontal red line in Figure 5.2) excludes any object that has <100 total observations, as variability is difficult to detect with fewer data points. A third cut (vertical green line in Figure 5.2) has also been made at 17 V mag. Objects fainter than this have unacceptably large photometric uncertainties making detection of all but the most extreme variability difficult. With these three cuts in place we are left with a total of 34772 objects to analyse for variability.

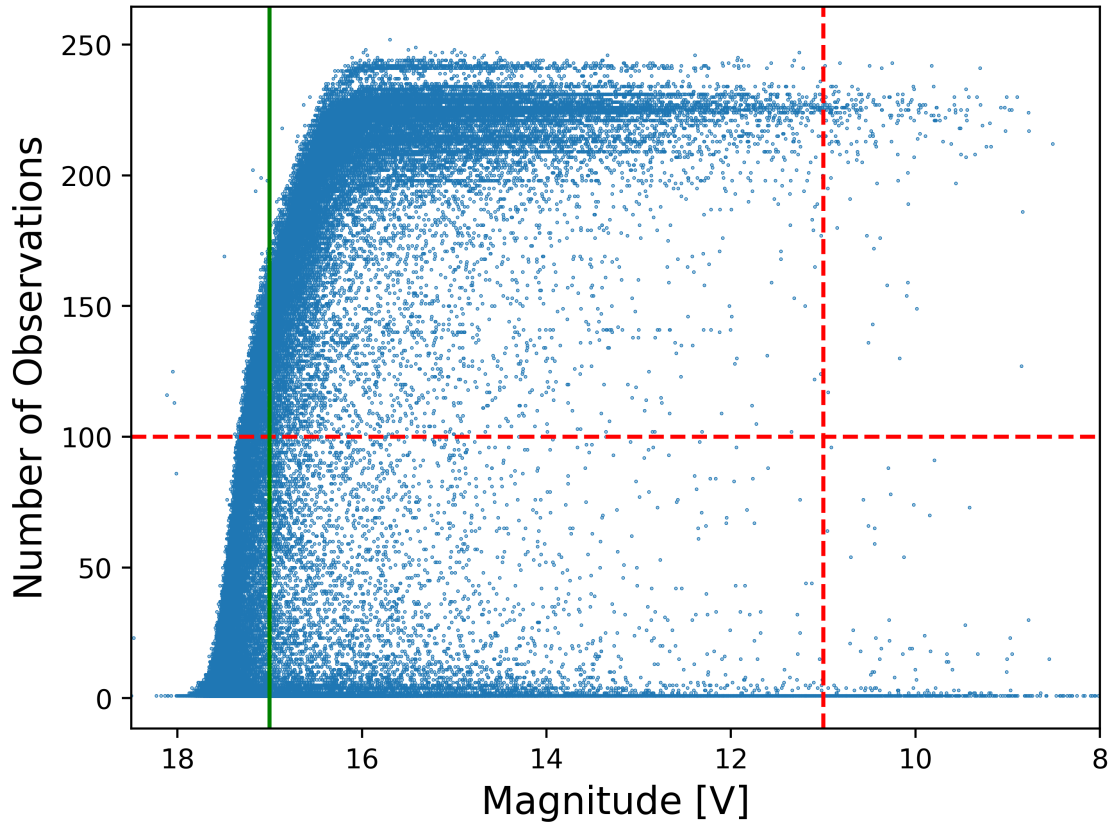


Figure 5.2: Each object detected has been plotted using its corrected magnitude and total number of observations.

5.4 Finding Variability

To find variability within the reduced data sample we first need to know what is not a variable. With this we can create lists of non-variable stars which will be used for differential photometry. First each object was binned by magnitude, from 11-17 V mag in 1 V mag bins. The standard deviation of the differential magnitude for each object is calculated for the duration of the observations. The standard deviation for the standard deviation in magnitude for each object within the 1 V mag bins is then calculated. This gives us the σ value for what we consider to be a non-variable for each magnitude of star. With the standard deviation calculated for each bin we

CHAPTER 5

set a 3σ deviation as the lower limit of variability within our sample. Any object with $\geq 3\sigma$ deviation is considered to be a high probability variable. Using the 3σ deviation we have found 719 variable objects. The light curves for each object have been examined by eye and the best have been hand selected into a smaller subset for further investigation.

This is an iterative process where we first find objects that do not have a deviation $>1\sigma$. These are the stars what will become the differential photometry star when the process is repeated. Once the list of differential photometry stars is established for each tile the search for variables objects is possible for the $\geq 3\sigma$ variable objects detected post differential photometry.

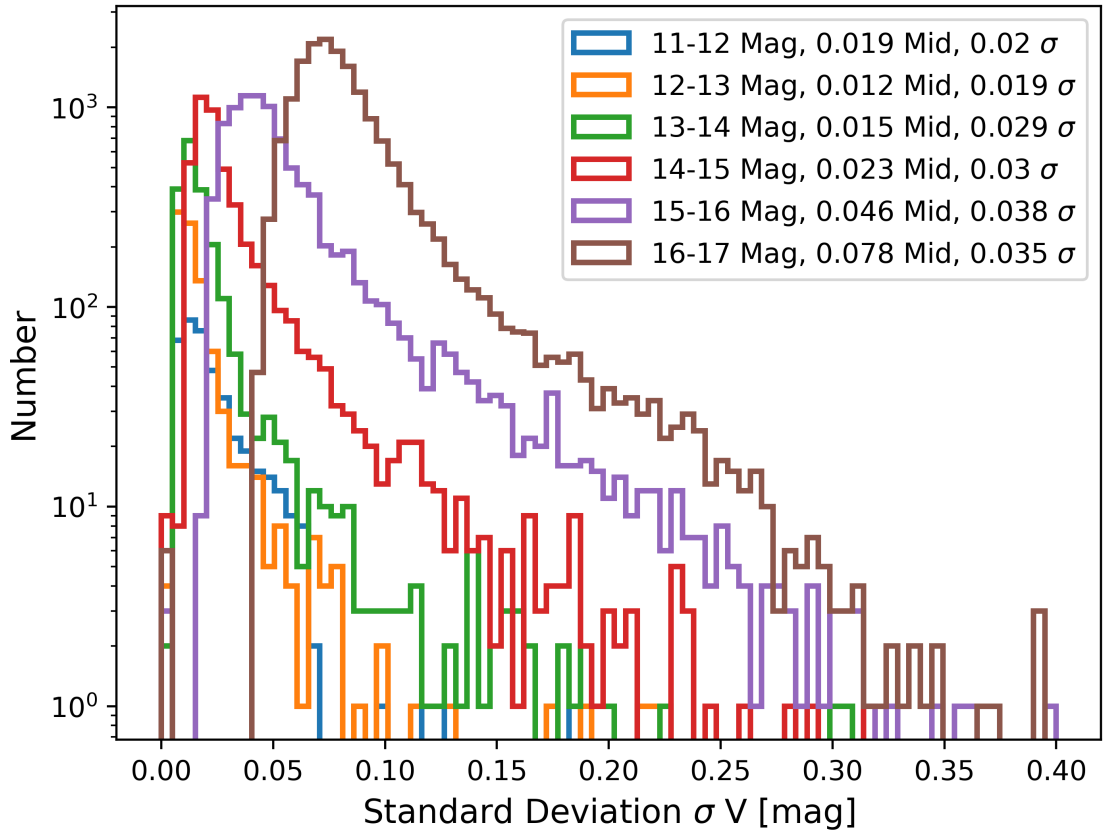


Figure 5.3: Histogram of the standard deviation for each object within the magnitude bins, with the deviation of the deviation within each been calculated.

Chapter 6

Discussion

During this masters project we have successfully initiated the MOSES survey, conducting 28 nights of observations, obtaining 4288 exposures (including overheads) requiring 71.5 hours of observing time. We have constructed a data pipeline, a photometric catalogue creation pipeline and begun the initial development of tools to find variable sources within the catalogue. When reducing the raw images taken with the MHT we encountered several issues. The first issue we had to overcome was the inaccurate WCS due to the very wide FOV of the MHT. This was successfully corrected for using an astrometry correction we developed using software from Astrometry.

The second issue we encountered whilst imaging with the MHT was that it suffers from noticeable vignetting, which leads to increasingly inaccurate photometric measurements as the distance from the centre of the field increases. To solve this we developed two techniques. The first was a vignette correction by comparing the magnitudes of a subset of the objects found within the UCAC4 Catalogue to give an initial zero-pointing which varies spatially across the field in order to account for the vignetting. Using this technique we are able to obtain an approximate on sky V band magnitude for each object. The second technique used to correct the vignetting was differential photometry. Although this did not produce a magnitude

CHAPTER 6

on a standard photometric system it produced more accurate photometric values which leads to an improvement in photometric accuracy when searching for variability especially for lower amplitude variability, which otherwise would be lost in the noise.

The catalogue creation script is a complete stand alone pipeline written to process the reduced images from the MHT. The script can correctly identify objects previously observed to create unique data files for all objects we have encountered during the MOSES survey. As the survey continues into a second season the number of available points for each object will increase which further enhances our ability to detect and correctly classify variable objects.

Given our experience over the previous year in Section 6.1 we suggest possible improvements which would increase our ability to detect smaller amplitude variability such as exoplanets.

6.1 Suggested Improvements to Survey Strategy

Due to being conducted on a telescope at relatively high latitude the MOSES survey has encountered some limitations not found by surveys conducted at more equatorial latitudes. In particular we are limited to a practical observing season of only around 8 months (September - April). Outside of this observing window nights become too short to allow practical observing by on-site observers. Within our limited observation season we have also been limited by the typically poor weather conditions found on the west coast of the UK. To improve our ability to detect variability we could modify the observing in a number of ways.

Currently the MHT requires an on-site observer to run the telescope, a future improvement to the MHT would therefore be to implement robotic observing, to obtain measurements any time the sky is clear, without the need for on-site observers. Preliminary estimates indicate that this should at least double the rate at which

CHAPTER 6

observations are obtained.

One obvious improvement to the MOSES survey would be to add a secondary telescope. The second telescope would be used to observe fainter objects within the survey field. By extending the practical magnitude range beyond V of 17 mag we would dramatically increase the number of detected objects. The second telescope would be set up to observe in the same way as the first telescope but instead of a 60s exposure time a 180-300s exposure time would be used. The increase in exposure time will increase the photometric accuracy of all objects in the survey field at the cost of reducing the observing cadence to ~ 90 minutes for the objects detected with the second telescope. The longer exposure time would not benefit any brighter objects as they would saturate or become nonlinear so there would be no photometric improvement. It also likely would not provide a significant improvement to the detection of exoplanet transits, due to the long delay between repeat observations, however it would significantly increase the numbers of fainter variables with periods >0.5 days detected.

Besides just exposing for longer the second telescope could also be used to carry out focused pointed observation on individual targets of interest within the individual tiles of the mosaic in order to for example provide high time resolution observations of a suspected exoplanet transit. However a second telescope is not fully required for this, using the MHT observations where you stay on a single tile to help constrain parameters such as the timing of a binary star eclipse. This can be done with the current setup (at the cost of losing observations of the other 15 tiles), but would obviously be better if done with a second dedicated telescope.

The 4 x 4 mosaic used to image the field has been successful in observing variability. The choice of a smaller field with a 3 x 3 array would increase the number of observations per object and reduce the observation cadence down to ~ 15 minutes, however we would not detect a large number of the object seen in the current survey.

CHAPTER 6

The number of objects with >200 observations would decrease to $\sim 17,000$ in a 3×3 array. If the survey was redesigned to a 5×5 array as mentioned before the observing cadence would become ~ 90 minutes, with an increase in objects with >200 observations to $\sim 47,000$. With a 90 minute cadence detection of short period, or short duration events (such as exoplanet transits) would become increasingly difficult. Therefore we consider the basic structure of the survey, the number of tiles and exposure time to remain optimum as we continue the survey. Though as discussed, in the future we may at times switch to focus on observing individual tiles during predicted events like eclipsing binary minima, or exoplanet transits.

6.2 MOSES Season 1

The MOSES survey has had a successful first season of observation, with the start of the second season in September 2019. During the first season of the MOSES survey 87,397 unique objects have been detected and catalogued into our Master Catalogue, each with unique data files to be analysed for variability. From this very large number of unique objects 29,399 have been observed >200 times. Objects with such high numbers of repeat observations are suitable for examination for variability. Of the objects with 200 or more individual photometric measurements we have found 719 which display variability at a level $\geq 3\sigma$ greater than that expected from photometric uncertainties alone. Visual examination of this subsample demonstrates that 60% appear to display genuine variability. It appears that the remaining 40% of apparent variables are actually due to problems with the photometric pipeline. In particular we have found that our differential photometry does not always locate the same differential star, which can affect the resulting light curve. This issue will be fixed in the next iteration of the pipeline. Also due to further inspection of our light curves the differential photometry star used will have to have a V mag 12-14.5 to ensure there is no nonlinearity within these objects. This is an issue

CHAPTER 6

that will be resolved in future upgrades to the catalogue pipeline. A subsample of the confirmed variable sources can be found in Appendix B. The following sections present examples of several newly detected variables found by the MOSES survey, as a demonstration of the potential of this survey to contribute to the study of several types of variable star.

6.3 Eclipsing Binary

Figure 6.1 is an example of an eclipsing binary star system found during the first season of the MOSES survey. When the light curve has been folded over the period 3.69 days there are two distinct dips in luminosity. This is the characteristic shape of a binary system as shown in Figure 1.9. At least 5 eclipsing binaries have been detected to date, with further examples showing in Appendix B. Previously there were no known eclipsing binaries within the survey field.

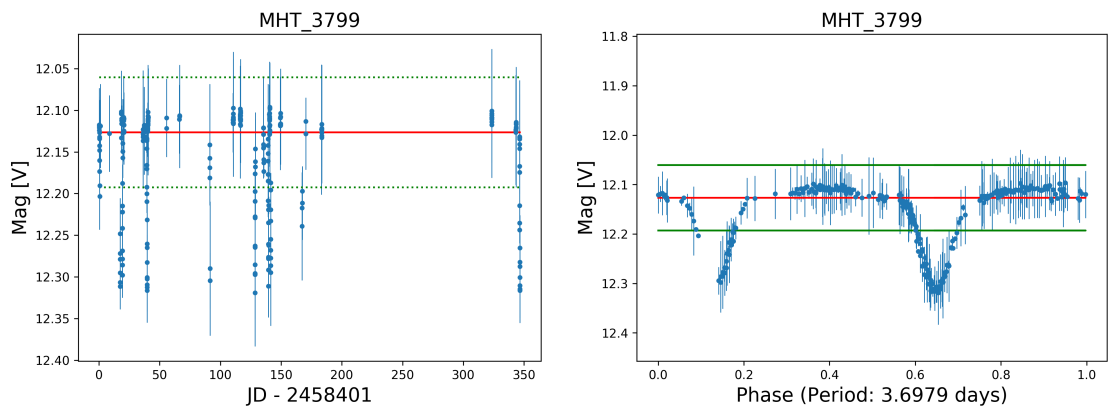


Figure 6.1: The light curve for object MHT 3799 and the folded light curve over a period of 3.69 days. The red line indicates the median V mag, with the green line the standard deviation above and below the median V mag.

6.4 Cepheid

Figure 6.2 appears to be new Cepheid variable. The object does appear to have the distinct saw-tooth shape used to identify Cepheids although it is not perfectly clear. The light curve is currently not very well sampled but with the continuation of the MOSES survey into season two the new data will allow for an improved light curve folding and period calculation. This should allow an unambiguous classification to be made.

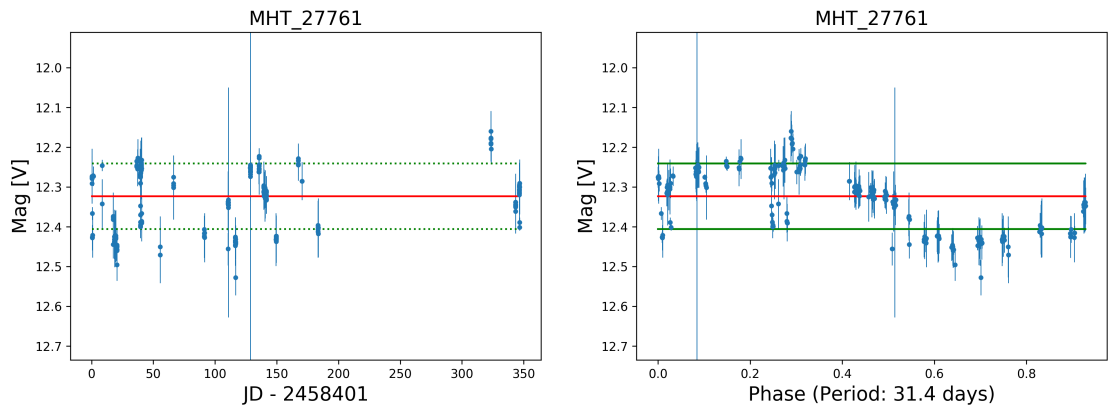


Figure 6.2: The light curve for object MHT 27761 and the folded light curve over a period of 31.4 days. The red line indicates the median V mag, with the green line the standard deviation above and below the median V mag.

6.5 Mira

Figure 6.3 is an example of a long period variable star. As such its period is highly uncertain, as we have only observed a single period. The object has an estimated period of 330 days and a magnitude range greater than 1 V mag. Based on the classification scheme presented in Figure A.1 this star would fall into the category of a Mira type variable. With more observations of this object a more accurate measurement of the period can be calculated as well as multi-band photometry to

CHAPTER 6

be obtained by the MHT will allow the stellar type of the star to be determined, and hence to further constrain the type of variable.

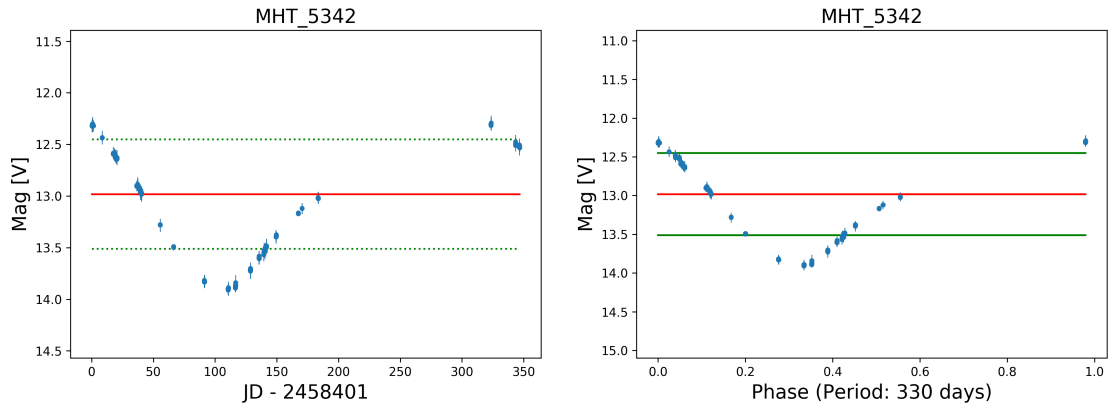


Figure 6.3: The light curve for object MHT 5342 and the folded light curve over a period of 330 days. The red line indicates the median V mag, with the green line the standard deviation above and below the median V mag.

6.6 Eclipsing Contact Binary

Figure 6.4 shows a new variable star within the survey field. Due to the unusual shape the classification of this object is still unclear but with more data collected as season two continues a classification may become possible. For this object we have calculated a period of 0.38628 days. Based on this unique shape we believe that this object may be a eclipsing contact (ECB) binary as the curved arch shape of the light curve is similar to that of an ECB.

CHAPTER 6

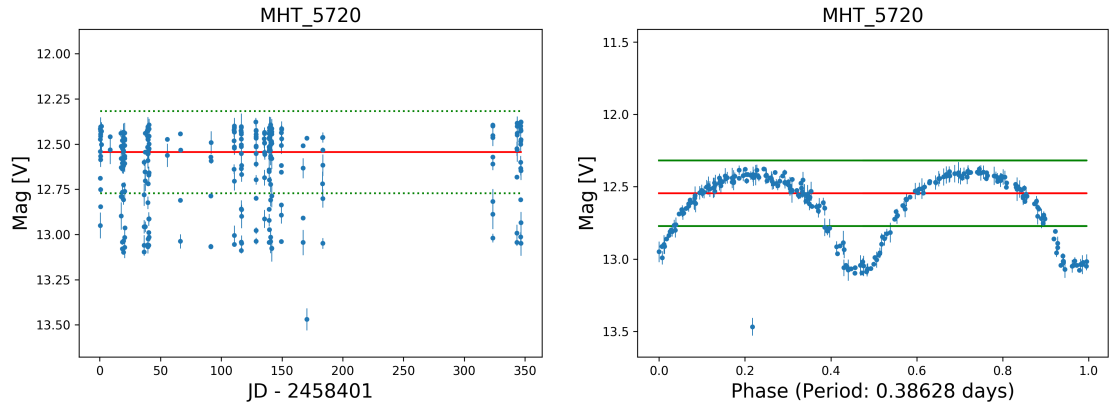


Figure 6.4: The light curve for object MHT 5720 and the folded light curve over a period of 0.3862844 days. The red line indicates the median V mag, with the green line the standard deviation above and below the median V mag.

6.7 Unknown Variability

Figure 6.5 appears to be a new interesting variable object. The light curve shows variability with a period of 0.50682 days. When the light curve is folded over this period there are also noticeable secondary dips in the light curve. It is unclear what causes the secondary dip feature of the light curve but it may possibly be due to a type of variable star that is in a binary system with a planet or another star causing the periodic dips in luminosity but this cannot yet be confirmed as additional observations are required.

CHAPTER 6

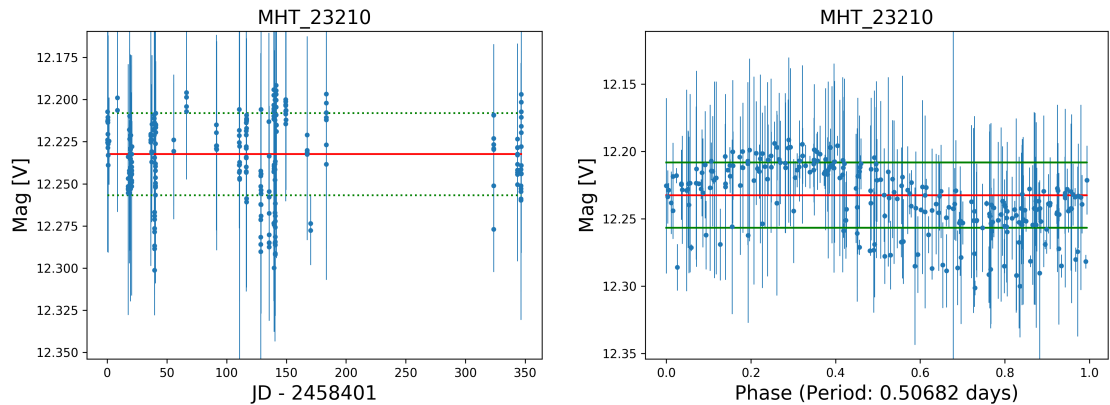


Figure 6.5: The light curve for object MHT 23210 and the folded light curve over a period of 0.50682 days. The red line indicates the median V mag, with the green line the standard deviation above and below the median V mag.

These objects are just the first of many variable objects found that have not yet been classified. For objects which appear to have periods >180 days it is not yet possible to accurately constrain their periods. As the survey continues and the number of data points increases it will become possible to identify the longer period objects. The MOSES survey has shown that it does detect variability and with enough time for analysis object types can be determined. With the absence of TESS observing the same region as MOSES there is the opportunity for many new exciting discoveries to be made by the MOSES survey, and its future undergraduate observers.

Chapter 7

Conclusion

The planning and the instigation of the MOSES survey has been successful. At present the survey has completed a first season of observations from October 2018 to April 2019, and is currently commencing the second season starting in September 2019. So far the survey has detected 87,397 unique objects. Amongst these object we have found 719 variable objects. This is a huge increase over the two previously known variables located in the MOSES survey field. However this is only the very beginning of what will be found. With future undergraduate and postgraduate projects the number of variable objects found with MOSES will increase as the sensitivity to lower amplitude variability increases due to improvements in data analysis, and the increasing timeline of available observations.

7.1 Future Work

Continuation of this survey will only increase the number of observations for the objected detected so far. With a second observation season the baseline of observations will increase which will aid in the survey's ability to detect long period variables as with more periods observed the period can be calculated with a higher accuracy.

CHAPTER 7

This project has been the foundation that can lead on to many different undergraduate projects. As we have a very large data set, there are still many objects to search for variability. We have also detected moving objects within our survey. It has not been possible to study these in detail. A follow up undergraduate project could be to search for the moving objects within the field and measure the velocities at which they pass across the field.

Bibliography

- Aerts, C., Christensen-Dalsgaard, & J. Kurtz, D. W. 2010, *Asteroseismology* (Springer, Dordrecht)
- ANDOR. 2019, Apogee Aspen CG16M
- ANTF. 2018, Australia Telescope National Facility
- Astrometry.net. 2019, Astrometry
- Bertin, E. & Arnouts, S. 1996, *aaps*, 117, 393
- Borucki, W. J., Koch, D. G., Lissauer, J. J., et al. 2003, *Society of Photo-Optical Instrumentation Engineers (SPIE) Conference Series*, Vol. 4854, *The Kepler mission: a wide-field-of-view photometer designed to determine the frequency of Earth-size planets around solar-like stars*, ed. J. C. Blades & O. H. W. Siegmund, 129–140
- Brau, J. 2019, *Novae, Supernovae, and the Formation of the Heavy Elements*
- Bruton, D. & Stephen, F. 2007, *Eclipsing Binary Stars*, <https://web.archive.org/web/20070414144827/http://www.physics.sfasu.edu/astro/ebstar/ebstar.html>
- Catelan, M., Pritzl, B. J., & Smith, H. A. 2004, *apjs*, 154, 633
- Chen, R. 2018, *Kepler By the Numbers Mission Statistics*
- Chodas, P., Khudikyan, S., & Chamberlin, A. 2019, *NEO Basics*

Diffraction Limited. 2019, Aquire and process images
<http://diffractionlimited.com/product/maxim-dl/>

ER Services. 2018, Eclipsing Binary Diagram

Gilmore, G. 2004, *Science*, 304, 1915

Howell, S. B., Sobek, C., Haas, M., et al. 2014, *pasp*, 126, 398

Johnson, M. & Dunbar, B. 2018, Liftoff of the Kepler spacecraft,
<https://www.nasa.gov/missionpages/kepler/launch/index.html>

Karttunen, H., Kröger, P., Oja, H., Poutanen, M., & Donner, K. J., eds. 2007,
Observations and Instruments (Berlin, Heidelberg: Springer Berlin Heidelberg),
pp.67–68, 84

Kazmierczak, J. & Garner, R. 2019, NASA's TESS Shares First Science Image in
Hunt to Find New Worlds

Koupelis, T. 2010, *In Quest of the Universe.*, 6th edn. (Jones and Bartlett Titles in
Physical Science)

Leavitt, H. S. & Pickering, E. C. 1912, *Harvard College Observatory Circular*, 173,
1

Lenz, P. & Breger, M. 2005, *Communications in Asteroseismology*, 146, 53

Majaess, D., Turner, D., & Lane, D. 2009, *actaa*, 59, 403

NASA Exoplanet Institute. 2019, NASA Exoplanet Archive

NASA Exoplanet Institute, https://exoplanetarchive.ipac.caltech.edu/docs/counts_detail.html.
2019, NASA Exoplanet Archive

Planewave Instrument. 2019, CDK700 (0.7m CDK Telescope System),
<http://planewave.com/products-page/cdk700/0-7m-cdk-telescope-system/>

- Planewave Software. 2019, Planewave Software and Updates
<http://planewave.com/downloads/software/>
- Pollacco, D. L., Skillen, I., Collier Cameron, A., et al. 2006, *pasp*, 118, 1407
- Ratzloff, J. K., Corbett, H. T., Law, N. M., et al. 2019a, *pasp*, 131, 084201
- Ratzloff, J. K., Law, N. M., Fors, O., et al. 2019b, *pasp*, 131, 075001
- Ricker, G. R. & TESS Team. 2015, in American Astronomical Society Meeting Abstracts, Vol. 225, American Astronomical Society Meeting Abstracts #225, 202.01
- Samus, N. N., Kazarovets, E. V., Durlevich, O. V., Kireeva, N. N., & Pastukhova, E. N. 2009, *VizieR Online Data Catalog*, 1
- Star.uclan.ac.uk. 2018, Jeremiah Horrocks Institute - Alton Observatory
- Wenger, M., Ochsenbein, F., Egret, D., et al. 2000, *aaps*, 143, 9
- Williams, M. 2017, What is the Transit Method
- Zhu, C., Liu, R., Alexander, D., & McAteer, R. T. J. 2016, The American Astronomical Society

Appendix A

Appendix

Date	Observations	Moon Phase (%)	Min Max Seeing (")
2018/10/09	14	New/Set (0)	1.98 - 3.53
2018/10/10	3	Waxing Crescent (2)	2.23 - 3.18
2018/10/17	2	First Quarter (57)	2.25 - 2.95
2018/10/26	6	Waning Gibbous (96)	1.95 - 3.31
2018/10/27	7	Waning Gibbous (91)	1.78 - 3.86
2018/10/28	12	Waning Gibbous (83)	1.91 - 2.99
2018/10/29	12	Waning Gibbous (74)	1.99 - 3.08
2018/11/14	4	Waxing Crescent (40)	2.11 - 4.97
2018/11/15	5	First Quarter (49)	1.95 - 3.32
2018/11/17	20	Waxing Crescent (68)	2.33 - 5.16
2018/11/18	14	Waxing Gibbous (76)	1.87 - 3.20
2018/12/03	2	Waning Crescent (24)	1.90 - 2.68
2018/12/14	4	First Quarter (41)	2.11 - 3.38
2019/01/08	6	Waxing Crescent (6)	3.15 - 3.86
2019/01/27	12	Third Quarter (54)	2.17 - 3.49
2019/02/02	20	Waning Crescent (5)	2.54 - 3.67
2019/02/14	14	Waxing Gibbous (67)	2.64 - 5.33
2019/02/21	10	Waning Gibbous (92)	2.38 - 4.37
2019/02/25	17	Third Quarter (56)	2.29 - 5.15
2019/02/26	17	Third Quarter (48)	2.18 - 5.62
2019/02/27	9	Waning Crescent (40)	2.00 - 2.87
2019/03/07	10	Waxing Crescent (4)	2.04 - 2.79
2019/03/25	4	Waning Gibbous (76)	1.75 - 3.22
2019/03/28	2	Third Quarter (47)	3.80 - 5.03
2019/04/10	7	Waxing Crescent (26)	2.85 - 3.67
2019/08/28	8	Waning Crescent (5)	2.09 - 3.49
2019/09/17	10	Waning Gibbous (90)	1.90 - 3.86
2019/09/20	17	Waxing Crescent (66)	2.03 - 3.61
Total	268		

Table A.1: Table of the Nights Observed with the number of epochs each night, with the moon phase and a representative seeing for each night from season 1 and the beginning of season 2.

Object_Name	RA (J2000)	Dec (J2000)
MHT_1	32.99822	62.74332
MHT_2	32.99278	62.41020
MHT_3	33.00609	62.77190
MHT_4	33.00441	62.58231
MHT_5	33.00542	62.57907
MHT_6	33.00507	62.69002
MHT_7	33.00826	62.70945
MHT_8	33.00144	62.33240
MHT_9	33.00820	62.61904
MHT_10	33.00520	62.44001
MHT_11	33.01294	62.73181
MHT_12	33.01284	62.65187
MHT_13	33.01348	62.70339
MHT_14	33.00867	62.47388
MHT_15	33.01419	62.76459
MHT_16	33.00045	62.65355
MHT_17	33.00195	62.45933
MHT_18	33.00325	62.76622
MHT_19	33.00106	62.46428
MHT_20	32.99404	62.58531

Table A.2: Example of the data stored in the Master Catalogue.

Object Name	JD	RA		Dec		Aper		Auto		Aper		Auto		Aper		Auto	
		J2000	ds	J2000	ds	Mag	Mag Err	Mag	Mag Err	Mag	Mag Err	Mag	Mag Err	Mag	Mag Err	Mag	Mag Err
MHT-1	2458401.306	32.9982	62.7433	-12.1037	-12.5175	0.0023	0.0038	13.3831	13.3424	32.7211	62.7562	-12.3529	0.0056	-12.7588	0.0086	13.0884	13.0829
MHT-1	2458401.325	32.9981	62.7433	-12.1992	-12.5226	0.002	0.0033	13.3728	13.3456	32.7211	62.7562	-12.4244	0.0342	-12.7649	0.0416	13.0968	13.0902
MHT-1	2458401.343	32.9982	62.7433	-10.249	-10.3891	0.0117	0.0169	13.3758	13.3312	32.7212	62.7562	-12.6088	0.0181	-12.7838	0.0264	13.1104	13.0952
MHT-1	2458401.361	32.9982	62.7433	-10.1202	-10.3457	0.0129	0.0178	13.3869	13.3345	32.7212	62.7562	-12.4836	0.0462	-12.7872	0.0589	13.1107	13.0862
MHT-1	2458401.379	32.9982	62.7433	-8.2204	-8.2662	0.0725	0.0753	13.3709	13.3232	32.7212	62.7562	-12.6084	0.0174	-12.7965	0.0251	13.1321	13.1058
MHT-1	2458401.404	32.9983	62.7433	-9.1392	-9.255	0.0304	0.0408	13.3706	13.3352	32.7212	62.7562	-12.5336	0.0268	-12.8049	0.0360	13.1173	13.0961
MHT-1	2458401.526	32.9981	62.7433	-9.1107	-9.1949	0.0291	0.0417	13.3878	13.3620	32.7210	62.7562	-12.6471	0.0034	-12.7529	0.005	13.0875	13.0829
MHT-1	2458401.546	32.9981	62.7432	-12.3742	-12.4784	0.0014	0.0023	13.3892	13.3598	32.7210	62.7562	-12.6485	0.0408	-12.7224	0.0425	13.0873	13.0911
MHT-1	2458401.577	32.9981	62.7433	-8.3108	-8.4354	0.0615	0.0772	13.3832	13.3335	33.0958	62.7127	-12.4809	0.0451	-12.735	0.051	13.1066	13.0916
MHT-1	2458401.597	32.9981	62.7433	-8.283	-8.6356	0.0635	0.087	13.3820	13.3495	33.0959	62.7127	-12.4653	0.0071	-12.6711	0.0104	13.1187	13.1060
MHT-1	2458401.615	32.9981	62.7432	-10.706	-10.7997	0.0067	0.0094	13.3772	13.3590	33.0959	62.7127	-12.5752	0.0404	-12.6975	0.0501	13.1093	13.0981
MHT-1	2458401.633	32.9981	62.7432	-9.9506	-10.0978	0.0136	0.0180	13.3853	13.3436	33.0959	62.7127	-12.5102	0.0544	-12.6802	0.0733	13.1147	13.0943
MHT-1	2458401.653	32.9981	62.7432	-9.3147	-9.6424	0.0249	0.0361	13.3893	13.3329	33.0959	62.7126	-12.4202	0.0188	-12.6657	0.0251	13.1209	13.0993
MHT-1	2458401.671	32.9981	62.7432	-8.3162	-8.3535	0.0632	0.0902	13.3862	13.3424	33.0959	62.7127	-12.4494	0.0122	-12.679	0.0166	13.1256	13.1046

Table A.3: An example of the data stored for each objected detected along with the corresponding zero point star data. JD = Julian date of observation. RA and Dec = Object location per observation. Aper Mag = Aperture magnitude vaule, Auto Mag = Automatic magnitude value. ds = differential star values, dszp = differential star post zero-pointing.

Class name adopted here	Other names in the literature	Mode Type	Period Ranges	Amplitudes (brightness)	Amplitudes (velocity)	log T_{eff} (K) approx. range	log L/L_{\odot} approx. range
Solar-like pulsator	main sequence	p	3 to 10 min	few ppm	$< 50 \text{ km s}^{-1}$	[3.70, 3.82]	[-0.5, 1.0]
	red giants	p	few hours	few 10 ppm	few ms^{-1}	[3.65, 3.70]	[-0.5, 2.0]
γ Dor	slowly pulsating F	g	8 h to 5 d	$< 50 \text{ mmag}$	$< 5 \text{ km s}^{-1}$	[3.83, 3.90]	[0.7, 1.1]
δ Sct	SX Phe (Pop. II)	p	15 min to 8 h	$< 0.3 \text{ mag}$	$< 10 \text{ km s}^{-1}$	[3.82, 3.95]	[0.6, 2.0]
roAp	—	p	5 to 22 min	$< 10 \text{ mmag}$	$< 10 \text{ km s}^{-1}$	[3.82, 3.93]	[0.8, 1.5]
SPB	53 Per	g	0.5 to 5 d	$< 50 \text{ mmag}$	$< 15 \text{ km s}^{-1}$	[4.05, 4.35]	[2.0, 4.0]
β Cep	β CMa, ζ Oph (SpT O) 53 Per	p&g	1 to 12 h (p)	$< 0.1 \text{ mag}$	$< 20 \text{ km s}^{-1}$	[4.25, 4.50]	[3.2, 5.0]
			few days (g)	$< 0.01 \text{ mag}$	$< 10 \text{ km s}^{-1}$		
pulsating Be	λ Eri, SPBe	p&g	0.1 to 5 d	$< 20 \text{ mmag}$	$< 20 \text{ km s}^{-1}$	[4.05, 4.50]	[2.0, 5.0]
pre-MS pulsator	pulsating T Tauri	p	1 to 8 h	$< 5 \text{ mmag}$			
	pulsating Herbig Ae/Be	p	1 to 8 h	$< 5 \text{ mmag}$			
	pulsating T Tauri	g	8 h to 5 d	$< 5 \text{ mmag}$			
p-mode sdBV	EC14026, V361 Hya	p	80 to 800 s	$< 0.1 \text{ mag}$		[4.20, 4.50]	[1.2, 2.2]
g-mode sdBV	PG1716+426, Betsy star, lpsdBV	g	0.5 to 3 h	$< 0.01 \text{ mag}$		[4.40, 4.60]	[1.2, 2.6]
PNNV	ZZ Lep, [WCE]	g	5 h to 5 d	$< 0.3 \text{ mag}$			
GW Vir	DOV, PG1159	g	5 to 80 min	$< 0.2 \text{ mag}$		[4.80, 5.10]	[1.5, 3.5]
DBV	V777 Her	g	2 to 16 min	$< 0.2 \text{ mag}$		[4.40, 4.60]	[-1.0, 0.7]
DAV	ZZ Ceti	g	0.5 to 25 min	$< 0.2 \text{ mag}$		[3.95, 4.15]	[-2.6, -2.2]

(a) The names and basic properties of main sequence, giant and compact pulsators (Aerts et al., 2010).

Class name adopted here	Other names in literature	Mode Type	Period Ranges	Amplitudes (brightness)	Amplitudes (velocity)	log T_{eff} (K) approx. range	log L/L_{\odot} approx. range
RR Lyr	RRab	F	$\sim 0.5 \text{ d}$	$< 1.5 \text{ mag}$	$< 30 \text{ km s}^{-1}$	[3.78, 3.88]	[1.4, 1.7]
	RRc	FO	$\sim 0.3 \text{ d}$	$< 0.5 \text{ mag}$	$< 10 \text{ km s}^{-1}$		
	RRd	F+FO	0.3 to 0.5 d	$< 0.2 \text{ mag}$	$< 10 \text{ km s}^{-1}$		
Type II Cepheid	W Vir	F	10 to 30 d	$< 1 \text{ mag}$	$< 30 \text{ km s}^{-1}$	[3.70, 3.90]	[2.0, 4.0]
	BL Her	F	1 to 5 d	$< 1 \text{ mag}$	$< 30 \text{ km s}^{-1}$		
RV Tauri	RVa, RVb	F?	30 to 150 d	$< 3 \text{ mag}$	$< 30 \text{ km s}^{-1}$	[3.60, 3.90]	[3.2, 4.2]
Type I Cepheid	—	F	1 to 50 d	$< 1 \text{ mag}$	$< 30 \text{ km s}^{-1}$	[3.55, 3.85]	[2.0, 5.5]
	s-Cepheid	FO	$< 20 \text{ d}$	$< 0.1 \text{ mag}$	$< 10 \text{ km s}^{-1}$		
Mira	SRa, SRb	$l = 0$	$> 80 \text{ d}$	$< 8 \text{ mag}$		[3.45, 3.75]	[2.5, 4.0]
	SRc	$l = 0$	$> 80 \text{ d}$	$< 1 \text{ mag}$			
	SRd	$l = 0$	$< 80 \text{ d}$	$< 1 \text{ mag}$			
PVSG (SpT A)	α Cyg	g,S?	10 to 100 d	$< 0.3 \text{ mag}$	$< 20 \text{ km s}^{-1}$	[3.45, 4.00]	[2.5, 4.5]
PVSG (SpT B)	SPBsg	g	1 to 10 d	$< 0.3 \text{ mag}$	$< 20 \text{ km s}^{-1}$	[4.00, 4.50]	[4.3, 5.8]
LBV	S Dor	g,S	2 to 40 d	$< 0.1 \text{ mag}$		[3.80, 4.20]	[5.5, 6.5]
WR	WC, WN	g,S	1h to 5 d	$< 0.2 \text{ mag}$		[4.40, 4.70]	[4.5, 6.0]
HdC eHe	R CrB	g?	40 to 100 d	$< 0.05 \text{ mag}$	$< 10 \text{ km s}^{-1}$	[3.50, 4.20]	[3.5, 4.5]
	PV Tel	S	$\sim 20 \text{ d}$				
	V652 Her	g,S?	$\sim 0.1 \text{ d}$				
	V2076 Oph	g,S?	0.5 to 8 d				

(b) The names and basic properties of supergiant pulsators (Aerts et al., 2010).

Figure A.1: The two tables used to aid the classifications of variable objects seen within the MOSES survey.

Appendix B

Variable Light Curves

Appendix B present the light curves for the variable objects that have been detect during the MOSES survey. Along with the light curves for the objects there are also preliminary period estimations with an attempt to phase fold the some light curves. With each light curve there are three horizontal lines superimposed. The red line represents the median V magnitude for each object. The green lines represent the standard deviation above and below the median value for each object.

